Arch. Metall. Mater. **70** (2025), 4, 1983-2001

DOI: https://doi.org/10.24425/amm.2025.156285

A. ARI[1*], T. KARAGÖZ[2], A. BAYRAM[3]

PROCESS OPTIMIZATION AND EFFECT OF POST-PROCESSING ON MECHANICAL PROPERTIES IN THE PRODUCTION OF Ti6Al4V ALLOY BY LASER METAL DEPOSITION METHOD

This study investigates the production and optimization of Ti6Al4V alloy, which is widely used in the aviation sector, by the laser metal deposition method. Despite the advantages of Ti6Al4V, such as high strength, low weight, and corrosion resistance, its production by laser metal deposition method is challenging due to the requirement of a controlled environment. The study examined the geometric structures and porosity values of the samples produced using 12 different process parameters. The number of experiments was reduced, and the most effective parameters were determined using the response surface method and ANOVA. The lower, middle, and upper regions of the test samples produced with optimum parameters were examined separately, and it was determined that the lower regions showed higher strength. It was observed that the Hot Isostatic Pressing and heat treatment applied to the produced samples reduced the strength values but significantly improved ductility and reduced the porosity. In addition, cryogenic heat treatment was applied to the Hot Isostatic Pressing-treated samples to further increase mechanical performance. This process facilitated the completion of martensitic transformation and led to finer and more homogeneous precipitation of carbides while decreasing the porosity ratio and increasing the elongation at break. This study aims to develop the potential of this advanced manufacturing technique in the aerospace sector by comprehensively addressing the effects of process optimization and post-processing in the production of Ti6Al4V by the laser metal deposition method.

Keywords: Ti6Al4V; Laser Metal Deposition; Post-processing; Microstructure; Microhardness

1. Introduction

Laser Metal Deposition (LMD) is an additive manufacturing process in which a laser beam is used as the energy source, injecting and melting metal powder with a gas stream, creating a molten pool on the surface of a metallic substrate. The main applications of LMD include repairing damaged parts, deposition of functional layers, and additive manufacturing of metal components. This free-form manufacturing process allows metal components to be produced directly from three-dimensional CAD files by adding materials layer by layer. The metal powder is often fed coaxially into the molten pool by an additional carrier gas [1]. To prevent oxidation, the molten pool must be protected from the atmosphere. Therefore, LMD is usually performed in a process chamber filled with inert gas or locally protected by an inert gas stream [2]. LMD has several advantages over other deposition processes; for example, with lower heat input and a correspondingly smaller heat-affected zone, deformation can be significantly reduced, and the heat effect on the surface of the substrate can be minimized. In addition, higher cooling rates can positively affect material performance by creating a finer microstructure [3]. LMD processes offer many unique advantages over other additive manufacturing techniques, especially when a near-net shape structure is desired. For example, large parts that cannot be made with powder bed fusion processes can be produced using LMD techniques [4]. In addition, LMD techniques are highly efficient when repairing damaged or worn parts or adding new features to existing parts [5,6]. The other advantages of this manufacturing process are the ability to produce functionally graded materials, higher deposition rates, and a wider processing window for optimization of finished parts [7]. Titanium alloys are widely used in various fields, such as automotive, aerospace, and petrochemical industries, as well as offshore equipment and medical devices, due to their superior properties, such as high strength-to-weight ratio, high corrosion resistance, and biocompatibility [8]. Among these alloys, Ti6Al4V is one

[1] OSTIM TECHNICAL UNIVERSITY, DEPARTMENT OF WEAPON INDUSTRY TECHNICIAN, VOCATIONAL SCHOOL OF HIGHER EDUCATION, ANKARA, TÜRKİYE
[2] COŞKUNÖZ KALIP MAKINA SAN. VE TIC. A.Ş., BURSA, TÜRKİYE
[3] BURSA ULUDAG UNIVERSITY, DEPARTMENT OF MECHANICAL ENGINEERING, BURSA, TÜRKİYE

* Corresponding author: ali.ari@ostimteknik.edu.tr

of the most widely used due to its balance of material properties [9]. Ti6Al4V has a density of about 40% of that of steel yet offers the same strength as steel, thus providing advantages in weight savings, replacement costs, and life cycle costs. The stable, protective, and robust adhesive oxide film gives Ti6Al4V excellent corrosion resistance, providing a service life 15 times longer than steel in seawater [10,11]. As a result, a significant increase in the industrial use of Ti6Al4V has been observed in the last two decades [12]. For these reasons, LMD applications of Ti6Al4V are increasingly gaining attention in scientific and engineering fields [13].

In the LMD process, three main parameters, namely laser power, scanning speed, and powder feed rate, have the most significant impact on the quality of the deposits and constitute the essential process parameters [14]. However, other process parameters, such as laser beam energy distribution, amount and shielding gas and powder carrier gas, powder size, and powder injection angle, can also impact the quality of the deposits. It is essential to understand the relationship between the basic process parameters and to optimize the process by relating these relationships to the geometric shape of the deposits [15]. Size and geometry (height, width, and depth) play a critical role in determining the quality of the deposited part, and it is necessary to optimize the process parameters to achieve the desired geometry [16]. Optimizing the process parameters for single parts is usually done by trial and error; however, this process is expensive and time-consuming. Therefore, it is necessary to develop a method that can precisely predict the geometry of a single part. Numerical, regression and analytical models are used to predict coating geometries. Process optimization is required to achieve a strong metallurgical bond between the coating and the substrate, low dilution (10-20%), and a small heat-affected zone [17]. Various geometrical features, such as dilution, are analyzed to measure the coating quality. Evaluating dilution in the laser cladding process tries to verify the metallurgical bond between the substrate and the coating, where mechanical stress is essential. The microstructure is directly affected by dilution [18].

On the other hand, increasing the laser power causes a significant increase in the penetration depth, indicating that the laser power is the most effective factor in the penetration depth. Increasing the scanning speed increases the dilution percentage, while it has a negative effect on the coating height. Increasing the laser power directly increases the dilution percentage, while increasing the powder feed rate has the opposite effect [19].

This study has investigated the most up-to-date status of scientific studies on the LMD process of Ti6Al4V in recent years. The process parameters, macro and microstructure, heat treatment methods, and the mechanical properties that can be obtained have been discussed in this context. Zhang [20] and Liao [21] observed that many fine α colonies and irregular needle-like α' structures are easily formed during laser melt deposition. While the α colony hinders the movement of dislocations, the needle-like α' structure contains a high density of dislocations; this results in a titanium alloy with high strength but poor plasticity. Studies by Cui et al. have shown that β grain width has a limited effect on α morphology [21]. Methods such as adding trace alloying elements [22] or external auxiliary energy fields [23] can promote the formation of equiaxed grains by refining coarse β grains and thus increase tensile strength and plasticity [24]. However, the complexity of equipment and technology may hinder production efficiency.

On the other hand, heat treatment is a more straightforward and effective method to improve mechanical properties than parameter adjustments [25]. Tao et al. [26] observed that as a result of the applied heat treatment, the α phase became coarser and the aspect ratio decreased from 14.87 to 3.27. In addition, the thin and needle-shaped secondary α phase precipitated from the remaining β phase. They concluded that these microstructural changes significantly affected the mechanical properties of the material. While the average hardness value increased from 315.77 Vickers hardness to 345.18 HV, no significant change was observed in the yield and tensile strength values. The most striking development was the increase in the elongation value from 8.80% to 14.29%. Wang et al. [4] improved the anisotropy of Ti6Al4V produced by LMD with low-temperature annealing treatment, and little change was observed in the microstructure and tensile properties. Zou et al. [27] observed a decrease in the aspect ratio of the acicular α structure after high-temperature heat treatment, which increased plasticity and led to a decrease in strength of approximately 300 MPa. Li et al. [28] stated that solution aging after SLM can promote the transformation of acicular martensite into α lath, and microstructure coarsening leads to decreased strength and plasticity. These studies show that heat treatment can change the microstructure and increase mechanical properties; however, the methods used may not always balance strength and toughness. The study of Zhao et al. [29] revealed that the formation of axial α was promoted by multi-stage heat treatment of Ti6Al4V alloys, leading to a significant increase in plasticity and only a slight decrease in strength.

A distinctive contribution of this study is the integrated assessment of process parameter optimization and advanced post-processing strategies (HIP and cryogenic treatment) for LMDproduced Ti6Al4V. Employing a full factorial design in combination with Response Surface Methodology (RSM) and ANOVA, the work statistically models the influence of process parameters on porosity, efficiency, and dilution. Beyond process optimization, the systematic comparison of asbuilt, HIP-treated, and HIP + cryogenically treated samples establishes a direct correlation between microstructural transformations (α, β, α' martensite, and basket-weave morphologies) and mechanical performance. By coupling statistical optimization with metallurgical interpretation and industrial applicability, the study not only advances the understanding of phase transformation mechanisms in LMD-fabricated Ti6Al4V but also proposes a viable post-processing route to achieve a balanced combination of strength and ductility for aerospace and defense applications.

2. Materials and methods

2.1. Materials

The present study performed multi-layer laser cladding of Ti6Al4V Materials on AISI 1050 substrate (TABLE 1). The steel plate size was 300 mm × 150 mm × 20 mm. Before the study, chemical (TABLE 1) and physical (TABLE 2) analyses of Ti6Al4V powder material were performed and compared with nominal values. As a result of these analyses, it was seen that it complies with the determined standards. Fig. 1 illustrates the micrograph of the Ti6Al4V powder.

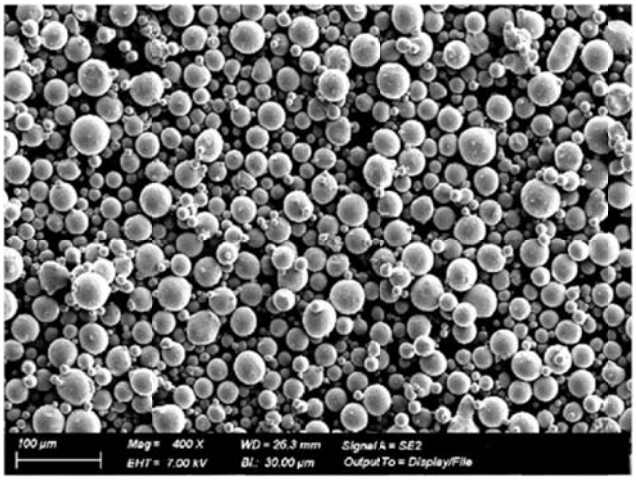

Fig. 1. SEM micrograph of the Ti6Al4V powder particles used in this study

2.2. Methods

The effects of key parameters on weld quality and powder usage efficiency were examined in detail. A single track of Ti6Al4V powder was deposited on the AISI 1050 steel substrate at laser powers of 1200, 1300, 1400, and 1500 W; laser scanning speeds of 6, 8, and 10 mm/s; and powder feed rates of 3.5, 4.0, and 4.5 rev/min. Ti6Al4V powder must be processed under a protective atmosphere in additive manufacturing systems to ensure uniform heat distribution and prevent oxidation. The oxygen level was reduced by feeding argon gas into the chamber. According to the literature, titanium LMD is performed at oxygen levels between 100 ppm and 3000 ppm (1000 ppm ≈ 0.1% oxygen). In this study, the argon flow rate was kept at 8 L/min, and the hatch spacing (pitch) was 1 mm. Each wall sample consisted of 10 layers with a layer height increment of 1 mm per layer.

The clad height, width, and penetration parameters were measured using Euromex ImageFocus ALPHA software. Two additional combined process parameters, Specific Energy Density (SED) and Powder Feeding Density (PFD), were introduced to explore their influence on cladding. Eqs. (1) and (2) define these combined parameters [30].

$$SED\left(\mathrm{J/mm^2}\right)=\frac{LP\left(\mathrm{W}\right)}{SS\left(\mathrm{mm/s}\right)\times d\left(\mathrm{m}\right)} \tag{1}$$

where SED is the specific energy density, LP is laser power, d is laser beam diameter, and SS is laser scanning speed.

$$PFD\left(\mathrm{rev/mm^2}\right)=\frac{PF\left(\mathrm{rev/min}\right)}{SS\left(\mathrm{mm/s}\right)\times d\left(\mathrm{m}\right)} \tag{2}$$

where PF stands for powder flow rate, d refers to the laser beam diameter, and SS represents the laser scanning speed.

When calculating efficiency (η), the mass of the amount of powder consumed in the elapsed time and the mass of the geometry produced are equalized. η can be found by weighing after each production and calculating how much of the spent powder solidifies and forms a layer. The macrostructure features of the single-track samples can be estimated by dilution rate (D), and they are calculated according to Eq. (3).

$$D\left(\%\right)=\frac{b\left(\mathrm{mm}\right)}{h\left(\mathrm{mm}\right)+b\left(\mathrm{mm}\right)}\times 100 \tag{3}$$

TABLE 1

Nominal chemical composition of Ti6Al4V material, according to ASTM F2924-14

Elements	Al	V	Fe	O	C	N	H	Y	Diğer	Ti
Min (wt.%)	5.50	3.50	—	—	—	—	—	—	—	Balance
Max (wt.%)	6.75	4.50	0.3	0.2	0.08	0.05	0.015	0.005	0.4	
Analysis results (wt.%)	6.47	4.06	0.13	0.14	0.01	0.01	0.003	0.001	0.1	

TABLE 2

Physical properties of Ti6Al4V powder material according to tests and analysis

Analysis	Specification			Conclusion	Conformity
Fluidity Analysis (ASTM-B213 Air, 23°C)	sec/50g (Hall)	≤30		24	+
Compressed (ASTM-B527)	g/cm^3	>2.8		3	+
Apparent Density (ASTM-B417)	g/cm^3	>2.45		2.48	+
Particle size distribution analysis by sieving (ASTM B214)	**Size µm**	**Min wt.%**	**Max wt.%**	**Conclusion**	**Conformity**
	+105	—	5	2.9	+
	–105+45	90	—	90	+
	–45	—	5	1.2	+

In this context, w denotes the width of the cladding layer (mm), *h* signifies the height of the cladding layer (mm), and *b* represents the depth of penetration relative to the surface (mm).

2.3. Test samples and measurements

The LMD process was carried out using a KUKA KR 90 R3100 ultra-6-axis industrial robot (Coşkunöz Holding, Bursa, TÜRKİYE). As shown in Fig. 2a, the system's main components include a laser, powder feeding unit, robot, LMD head, and a specially designed chamber to perform the process in an inert gas environment. Fig. 2b shows the sealed cabin design that provides a protective atmosphere for LMD.

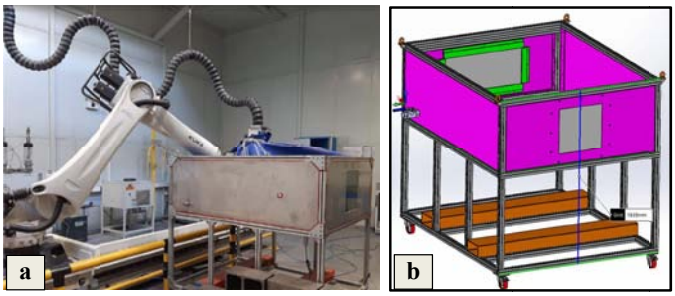

Fig. 2. a) Experimental setup and b) Protective cabin designed for the LMD process

Single-track samples were produced using 12 different parameter combinations (Fig. 3a). A 30 mm long tool path and 10 layers were used in each sample production. The 30 mm track length was kept the same (Fig. 3b). After every 3 layers, the process was paused until the temperature fell below 170°C before resuming deposition. Thus, samples were produced using the 3 layers + waiting + 3 layers + waiting + 4-layer strategy specified in Fig. 3c. The same production strategy was used for each parameter set. The width parameter (*w*) is defined as the average of the maximum and effective widths of the deposited track. The height is considered the total build height. Since the total height differs in each region, the h_o value was calculated as shown in Fig. 3c. The samples were cut in cross-section using wire Electrical Discharge Machining (EDM), then ground and polished. Cross-sections of the samples were prepared to analyze hardness and microstructure for each set of parameters. Microhardness was measured using a Vickers tester (HV 0.5) at a 50 g load and 10 s dwell time. For each of the 12 samples, microhardness was measured at 18 points. Hardness values were classified by layer level to examine the effect of layer height on microhardness, and horizontal hardness differences between layers were also evaluated. The strategy used for microhardness measurement is illustrated in Fig. 3d. The average values in sections A, B, and C were used to observe variations along the horizontal direction. In cyclic thermal processes such as LMD, microhardness can vary from layer to layer. Therefore, each sample was divided into 6 levels to determine hardness variation between layers.

After single-track multilayer deposition, a wall geometry was built using the optimum parameter set obtained from process optimization. Tool path and scanning direction are very important in building wall geometries; hence, the same directional tool path that provides the best cooling was chosen. This path was rotated 90° in each subsequent layer (Fig. 4a), minimizing geometric differences between layers.

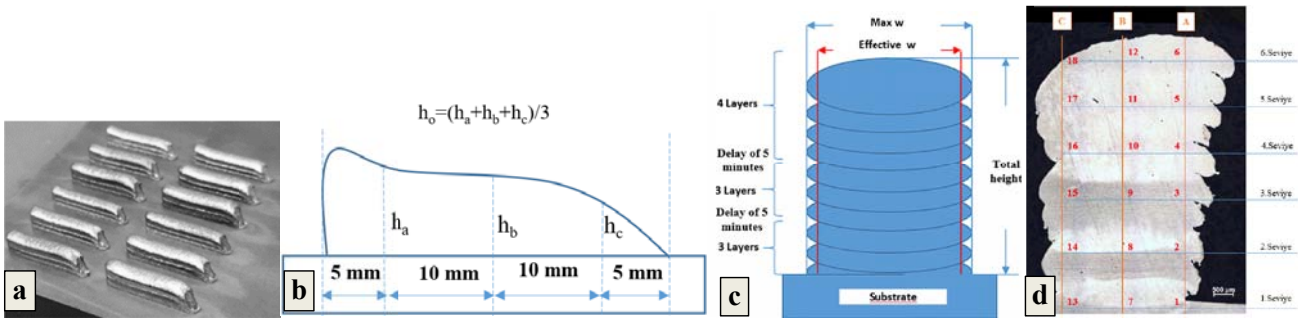

Fig. 3. a) Test samples b) Cross section of 10-layered sample, c) 10-layer sample strategy, d) Microhardness measurement strategy

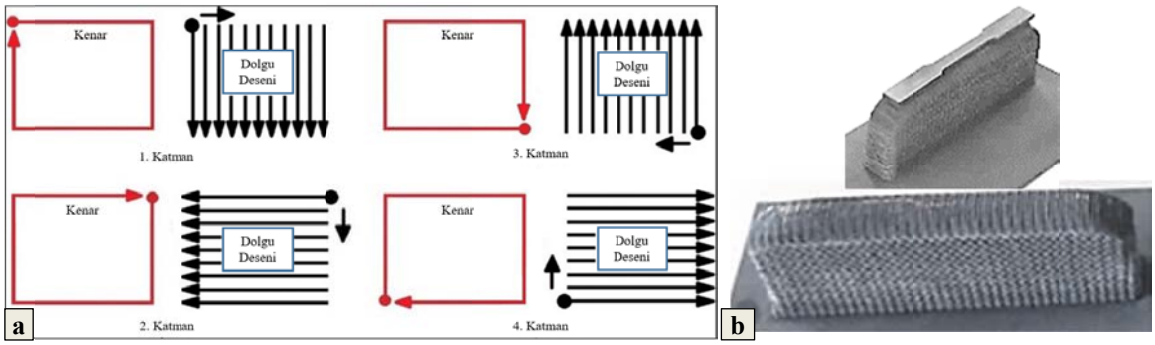

Fig. 4. a) Strategy used in wall geometry generation, b) Generated wall geometries, Orientation of samples extracted from generated walls

Tensile test samples were prepared according to DIN 50125 standard. To evaluate mechanical properties through the build height, three tensile specimens were extracted from the bottom, middle, and top regions of the wall produced with the optimum parameters. The tensile specimens were oriented parallel to the deposition direction (Fig. 4b). Wire EDM was used to remove the tensile specimens from the built wall.

2.4. Post-Processing

Hot Isostatic Pressing (HIP) and heat treatment (HT) were applied to the samples to eliminate porosity and tool path effects and to homogenize the microstructure. Additionally, the effect of cryogenic treatment on mechanical properties and microstructure was investigated.

There is no standard set of HIP and heat treatment parameters for the LMD process; different studies have used different conditions. The most commonly used parameters reported in the literature are 920°C, 100 MPa, and 2 hours. However, studies have shown that 200 MPa and 800°C are sufficient to eliminate porosities. When HIP is performed at higher temperatures, the microstructure coarsens and strength is reduced. Therefore, to achieve high strength, we applied HIP at 800°C and 200 MPa for 2 hours in this study. Fig. 5a shows the parameters for HIP and heat treatment.

In addition to HIP and furnace HT, cryogenic treatment was also applied. Cryogenic treatment involves cooling materials (using liquid nitrogen or helium) to very low temperatures. This process helps make the material's crystal structure more regular, reduce internal stresses, and produce a more homogeneous microstructure. Studies have found that cryogenic cooling improves surface integrity and chip morphology of titanium alloys, and that cryogenic treatment increases tool life and material removal rate in machining of titanium alloys. In a study by Arunprasath et al., cryogenic treatment of titanium caused a 2% decrease in yield strength but a 5.3% increase in plastic deformation. Although several studies have examined cryogenic treatment of titanium alloys, there are limited studies directly on their microstructure and properties. Therefore, this study investigated the effect of cryogenic treatment on the microstructure and tensile properties of Ti6Al4V. As strip samples were used, cooling was provided by liquid nitrogen. As shown in Figure 5b, samples were kept at –180°C for 24 h and 36 h; afterward, porosity measurements, microstructural examinations, and tensile tests were performed on these samples. Tensile specimens were taken from the bottom, middle, and top layers of each condition.

2.5. Experimental design

The full factorial Design of Experiment (DOE) is one approach to systematically determine how different input values affect output responses. The primary objective of DOE is to find the specific input values that optimize the outputs. A full factorial design was chosen over Taguchi or fractional factorial designs to achieve more accurate results. Although a full factorial design requires more resources and time (especially for 3 factors), it clearly identifies main effects and interaction effects on the response variables, providing higher accuracy. Therefore, as indicated in TABLE 3, a full factorial design with 3 factors and 3 levels (including replications and center points) was used to simultaneously investigate the effects of LP, SS, and PF on porosity, efficiency, and penetration.

TABLE 3

Parameters of samples produced process

Experiment No	LP (W)	SS (mm/s)	PF (rev/min)	SED (J/mm^2)	PFD (rev/mm^2)
S1	1200	6	3.5	66.7	0.19
S2	1200	8	4.0	50.0	0.17
S3	1200	10	4.5	40.0	0.15
S4	1300	6	3.5	72.2	0.19
S5	1300	8	4.0	54.2	0.17
S6	1300	10	4.5	43.3	0.15
S7	1400	6	3.5	77.8	0.19
S8	1400	8	4.0	58.3	0.17
S9	1400	10	4.5	46.7	0.15
S10	1500	6	3.5	83.3	0.19
S11	1500	8	4.0	62.5	0.17
S12	1500	10	4.5	50.0	0.15

In this study, the best parameter was obtained by using the Response Surface Method (RSM) for optimization. In addition, the effects of the parameters on the outputs were investigated separately. The RSM is an optimization method that uses experi-

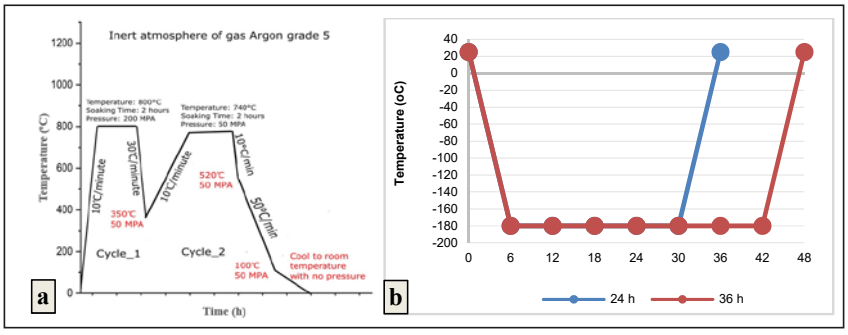

Fig. 5. a) HIP and HTparameters applied to the samples, b) Cryogenic HT parameters

mental design, regression models, and desirability functions [35]. The response surface method aims to explain the relationship between the input variables and the response variables and find the optimum parameters according to the desired functions with minimum trials [36]. The first step in obtaining the optimum results is to develop the relationship between the various process parameters and their corresponding responses. Here, a second-order regression model was used to fit the experimental data as described in Eq. (4) [37]:

$$Y = \beta_0 + \sum_{i=1}^{n} \beta_i \cdot x_i + \sum_{i=1}^{n} \beta_{ii} \cdot x_i^2 + \\ + \sum_{i=1}^{n-1} \sum_{j=i+1}^{n} \beta_{ij} \cdot x_i \cdot x_j + e \quad (4)$$

Here, "β_0" is the regression equation constant, "β_i and β_j" are the regression coefficients. The first and second sums represent the linear and polynomial terms, the third sum represents all input factors, and "e" represents the error. The fit of the regression models to the experimental data is evaluated by ANOVA analysis. The general procedure for parameter optimization is as follows: (a) select the design parameters and their limits; (b) develop a design matrix using a central composite design; (c) conduct experiments; (d) measure the porosity, efficiency, and penetration of the coated samples; (e) establish the mathematical model to relate the processing parameters to the results; (f) validate and verify the model; and (g) select the desirability method and obtain the optimal parameter set.

3. Results and Discussion

The cross-sectional profiles of the experimental samples produced according to the design matrix presented in TABLE 3 were analyzed, and the obtained geometry, porosity (%), penetration (μm), efficiency (%), average β grain size (μm), and microhardness (HV) values were measured. The measurement results of the experiment produced with 12 different parameter combinations are presented in TABLE 4.

3.1. Efficiency (η), cladding height (h) and dilution ratio (%D)

An experimental study was conducted to understand the effects of different process parameters on the physical properties of the samples. The data obtained were evaluated using statistical analysis. The findings presented in Fig. 6 reveal in detail the effects of combined parameters such as SED and PFD on the physical properties of the samples.

Efficiency was calculated as the ratio of the mass of the deposited material to the mass of powder consumed. As seen in Fig. 6a, a strong positive correlation was observed between efficiency and SED (R^2 = 0.8786), indicating that ~87.86% of the variability in efficiency can be explained by SED. In contrast, a weaker positive correlation was detected between efficiency and PFD (R^2 = 0.4512, Fig. 6b). In terms of efficiency, sample S10 (SED 83.3 J/mm^2) showed the highest value at ~80%, while sample S6 (SED 43.3 J/mm^2) showed the lowest at ~58%. Increasing SED by 40 J/mm^2 led to a 38% increase in efficiency. Examining the geometry, it was observed that SED and PFD had a positive effect on cladding height (Fig. 6c-d). Higher heat input increased powder deposition efficiency and thus increased the cladding height. The cladding height ranged from 6.9 mm in sample S6 to 8.9 mm in sample S10. Increasing SED by 40 J/mm^2 resulted in a 29% increase in height. The R^2 values showed that cladding height was 86% correlated with SED and 96% with PFD. Dilution rate (%D) is directly related to material flow and thermal input. An optimal melt pool depth is critical for uniform material deposition. The literature indicates that dilution rates between 10-20% are acceptable for laser-cladded surfaces [38]. As seen in Fig. 6e-f, increasing SED and PFD increased the dilution percentage [39]. Higher SED increased penetration depth and thus the dilution percentage due to greater heat input to the substrate. In this study, dilution percentage varied between 9.7% and 14.5%, all within acceptable limits. The highest dilution ratio (14.5%) was observed in sample S10 (SED 83.3 J/mm^2), while the lowest (9.7%) was in sample S12 (SED 50.0 J/mm^2). The relationship between PFD and dilution percentage was found to be quite weak ($R^2 \approx 0.05$).

TABLE 4

Measurement results of Experiment

Experiment No	Cross-sectional Porosity (%)	Average Porosity (μm)	Max Porosity (μm)	b (mm)	w (mm)	h (mm)	D (%)	η (%)	Average β Grain Size (μm)	Average hardness (HV)
S1	0.10	33.0	139.0	1.0	5,1	8.5	10.8	0.65	216.8	357.6
S2	0.20	20.6	118.8	1.1	4,7	7.5	12.8	0.62	191.0	363.3
S3	0.10	18.4	51.9	1.0	4,4	7.3	12.1	0.62	199.1	364.9
S4	0.04	14.8	60.0	1.4	5,4	8.8	13.3	0.70	206.4	360.3
S5	0.10	16.8	70.2	1.2	4,9	7.7	13.1	0.66	216.0	360.1
S6	0.10	19.3	98.0	1.0	4,3	6.9	12.7	0.58	203.1	363.2
S7	0.10	19.4	52.3	1.4	5,7	8.9	13.5	0.76	207.4	357.3
S8	0.10	18.0	43.1	1.3	5,1	7.8	13.9	0.69	211.7	359.8
S9	0.05	18.0	48.8	1.1	4,8	6.8	14.0	0.63	191.4	362.5
S10	0.03	18.0	41.8	1.5	6,1	8.6	14.5	0.79	219.2	361.0
S11	0.04	15.5	44.5	1.3	5,5	7.5	14.3	0.72	175.7	354.7
S12	0.10	11.9	90.9	0.7	5,2	6.9	9.7	0.69	205.1	358.7

As PFD increases, more powder interacts with the laser beam, reducing the heat reaching the substrate. Fluctuations in dilution percentage and track depth were related to changes in LP (Fig. 6g-h).

Fig. 7 and TABLE 5 present the ANOVA results for η, D and h. The p-values obtained for all models are less than 0.05, indicating that the proposed models are statistically significant at

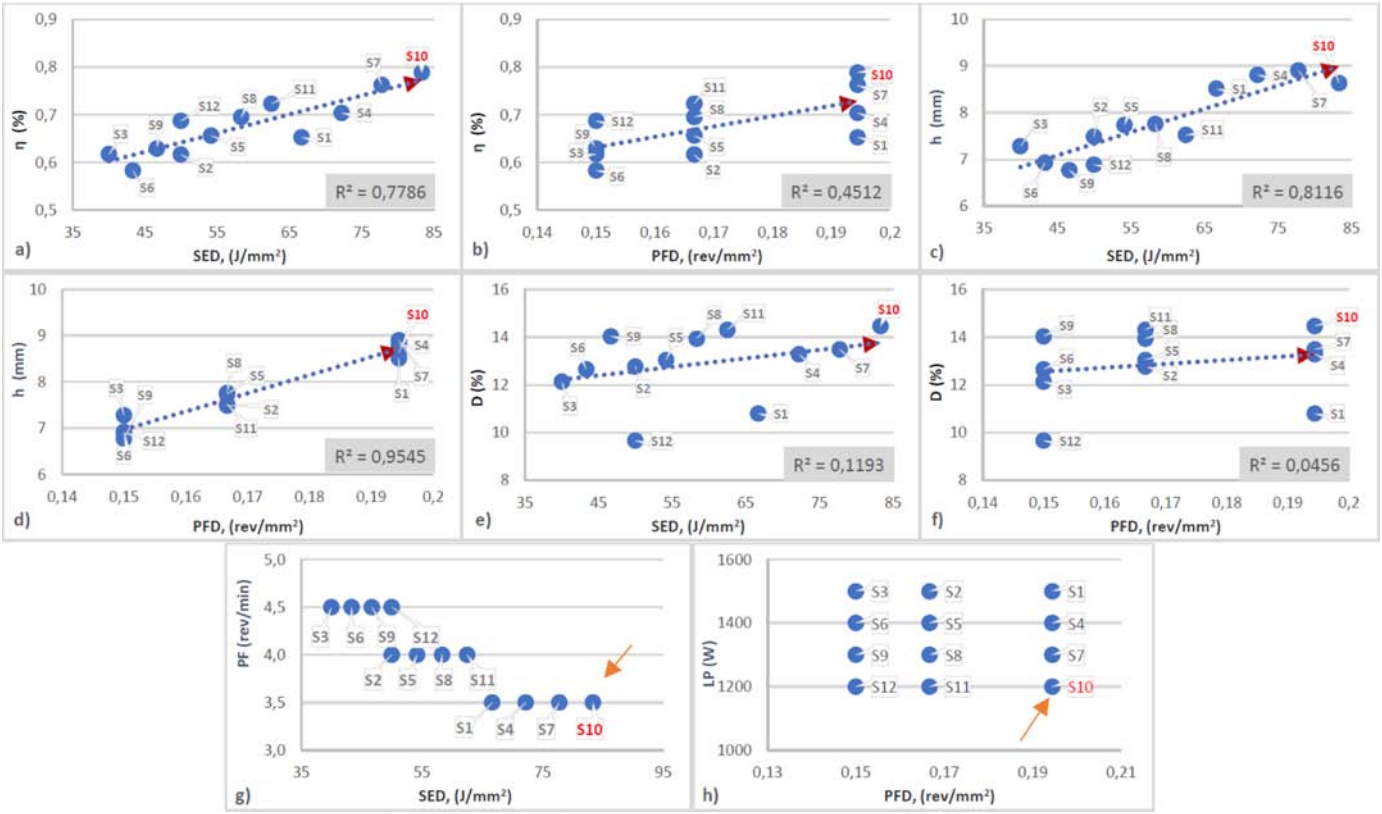

Fig. 6. Effect of SED and PFD on a) and b) η, c) and d) h and e) and f) %D g) fluctuation of PF with respect to SED h) fluctuation of LP with respect to PFD

TABLE 5

Results of ANOVA for η (%), D (%) ve h (mm)

S/N ratio	36.57	**Effectiveness of process parameters on η (%)**							
	Degrees of Freedom	Average S/N Values				Sum of Squares	Variance	F	Percentage of Contribution (%)
		Level 1	Level 2	Level 3	Level 4				
A – LP	3	35.97	36.20	36.82	37.28	3.22	1.07	1.66	22.14
B – Scan Speed	2	37.21	36.54	35.96		3.12	1.56	2.42	32.26
C – PF	2	37.21	36.54	35.96		3.12	1.56	2.42	32.26
Error	4					2.58	0.65		13.33
Total	11					6.88	4.84		100.00
S/N ratio	17.77	**Effectiveness of process parameters on *h* (mm)**							
	Degrees of Freedom	Average S/N Values				Sum of Squares	Variance	F	Percentage of Contribution (%)
		Level 1	Level 2	Level 3	Level 4				
A – LP	3	17.78	17.83	17.80	17.67	0.04	0.01	0.01	0.15
B – Scan Speed	2	18.81	17.65	16.86		7.67	3.84	2.10	40.31
C – PF	2	18.81	17.65	16.86		7.67	3.84	2.10	40.31
Error	4					7.32	1.83		19.24
Total	11					8.06	9.52		100.00
S/N ratio	22.15	**Effectiveness of process parameters on %*D***							
	Degrees of Freedom	Average S/N Values				Sum of Squares	Variance	F	Percentage of Contribution (%)
		Level 1	Level 2	Level 3	Level 4				
A – LP	3	21.49	22.27	22.81	22.01	2.72	0.91	0.72	21.16
B – Scan Speed	2	22.24	22.61	21.59		2.12	1.06	0.84	24.72
C – PF	2	22.24	22.61	21.59		2.12	1.06	0.84	24.72
Error	4					5.04	1.26		29.40
Total	11					12.01	4.29		100.00

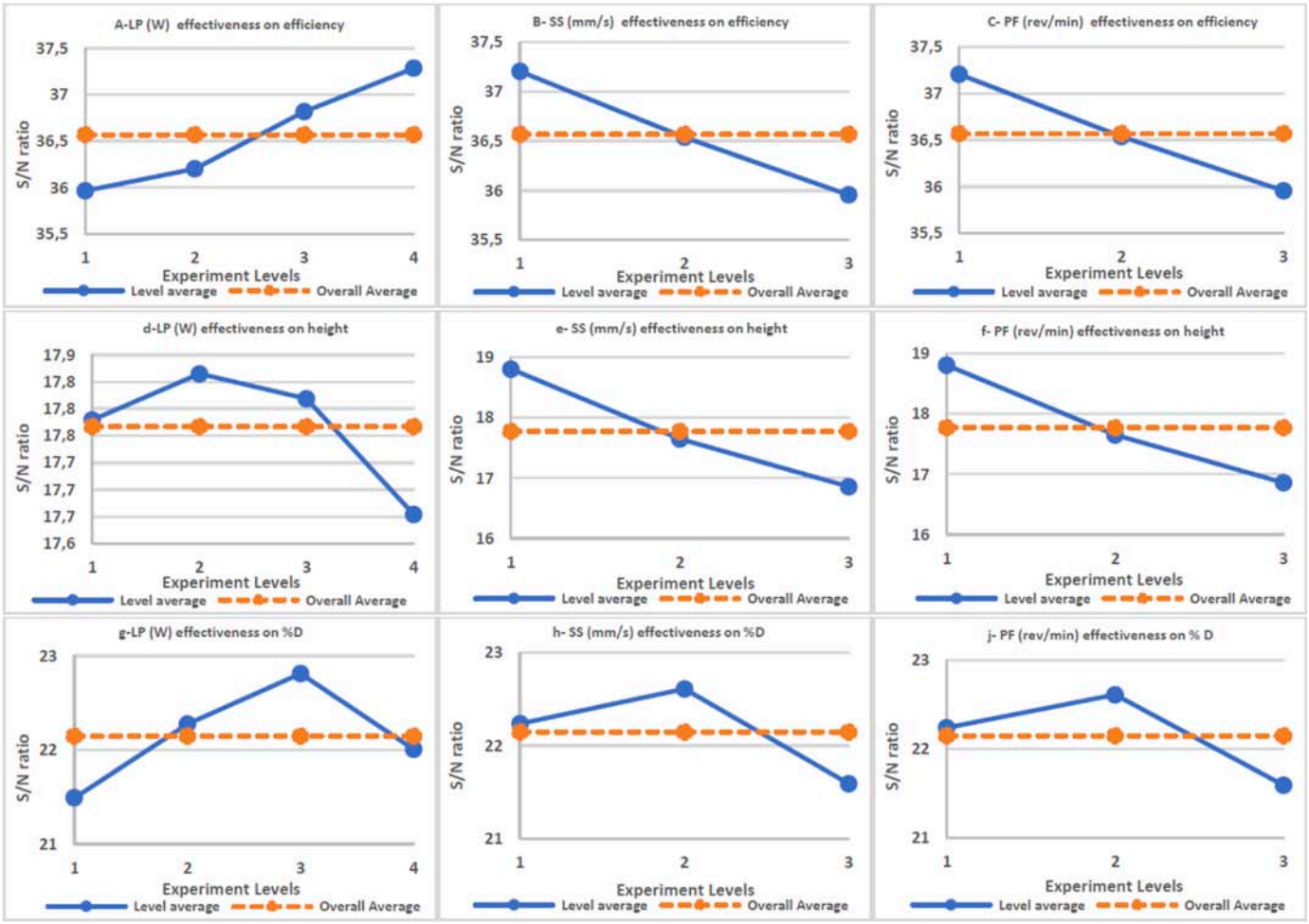

Fig. 7. Main effecs plot for η (%), D (%) ve h (mm)

a 95% confidence level. The effect sizes and significance levels of these factors were visualized using Pareto charts. Through a comprehensive analysis of the experimental responses, optimal empirical models were determined for each response. These models define the correlations between process parameters and the resulting properties, forming a basis for future optimization studies.

Fig. 7a shows the effect of LP (W), SS (mm/s) and PFD (rev/mm^2) parameters on the coating efficiency as a result of ANOVA analysis. In TABLE 5, the effects of coating parameters on efficiency are quantified as percentages. At fixed SS and PF, increasing the LP increased the coating efficiency by approximately 22%. For example, when the LP was increased from 1200W (S1) to 1500 W (S10) while keeping the SS of 6 mm/s and the PF of 3.5 constant, the efficiency increased by approximately 23%. On the other hand, the increase in SS and PF negatively affected the coating efficiency by approximately 32%.

Fig. 8 provides a mapping that can help in the selection of optimum production parameters for coating efficiency. Pareto analysis showed that over 76% efficiency was achieved at high LP (1500 W) and low SS (6 mm/s). It was also observed that the combination of low SS (6 mm/s) and low PF provided the highest efficiency. Increased powder splashing at high SS and excessive powder usage at high PF reduce efficiency. At low PF, efficiency increased with the increase in SED. When the

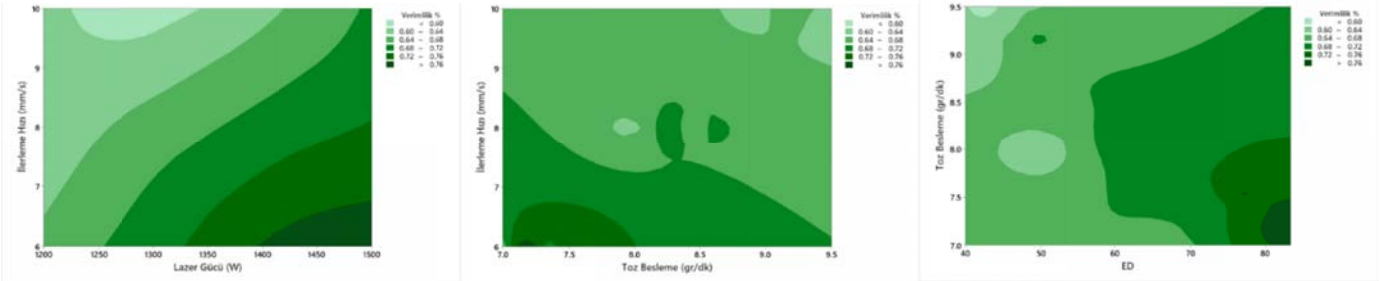

Fig. 8. Pareto analysis for efficiency factor

relationship between powder feed and energy density was examined, it was seen that the combination of low PF and high energy density provided the maximum efficiency. However, these conditions can cause overheating and lead to undesirable results such as crack formation on the part or separation from the substrate.

Fig. 7b shows the effect of LP (W), SS (mm/s) and PF (rev/min) parameters on the coating height as a result of ANOVA analysis. In TABLE 5, the percentage effects of these parameters on the coating height are quantified. The effect of LP was found to be fluctuating and quite weak at 0.15%. For example, when the LP was increased from 1200 W to 1500 W while keeping other parameters constant, the coating height increased by only 0.1 mm. In contrast, it was observed that the SS and powder feed rates had a negative effect of approximately 40%. The increase in these parameters decreased the coating height. The highest coating value (8.8 mm) was obtained in the S4 sample produced at 1300 W LP, 6 mm/s SS and 3.5 rev/min powder feed rate parameters. Fig. 7c shows the effect of process parameters on the dilution rate as a result of ANOVA analysis. The numerical values of these effects are given in TABLE 4. It was observed that all three parameters affected the dilution ratio approximately equally. It was found that at constant LP, the depth of the scan track decreased as the SS increased. At high SSs, the shallow penetrable zone caused poor surface spreading, which could lead to insufficient bonding to the previous layers and defects in the multilayer production process. The low height is a result of the partial evaporation and deep penetration of the melt due to the high-power output [40]. This situation can be associated with the increased heat transfer from the substrate surface to the interior. The increase in SED caused an increase in the coating depth and dilution percentage at constant PF. When the S3-S6-S9-S12, S2-S5-S8-S11 and S1-S4-S7-S10 samples were compared with each other, it was observed that the dilution ratio increased with the increase in the SED value at the same PF. However, despite having high LP of 1500 W, sample S12 showed poor surface spreading due to high SS.

Fig. 9 provides a mapping that can help in selecting the optimum manufacturing parameters for dilution ratio (%*D*). Pareto analysis showed that the highest dilution ratio will be obtained at high LP (1500W) and low SS (6 mm/s). It was also observed that the dilution ratio increased with the increase in SED at low powder feed rates.

3.2. Porosity

Fig. 10 shows the relationship between the porosity density, average porosity, and maximum porosity values of the samples with respect to SED and PFD. Observations show that porosity density decreases as SED and PFD increase (Fig. 10a-b), but the average porosity value increases slightly (Fig. 10c-d). The porosity densities of samples S4 and S10, which have the highest SED values, are the lowest at approximately 3%. The decrease in porosity density with increasing SED can be explained by the effect of higher energy input on melting and solidification. A high SED leads to more homogeneous melting and prevents gases from being trapped in the material, resulting in less porosity. For example, the porosity density of sample S2 (SED ~42.9 J/mm^2) is about 10 times higher than that of sample S10 (SED ~71.4 J/mm^2). Among samples with similar SED values (S1, S2, S3, S6, S7, S8), porosity densities were very close to each other.

Because evaluating only porosity percentage may overlook large isolated pores, the average porosity (Fig. 10c-d) and maximum pore size (Fig. 10e-f) were also analyzed. According to Fig. 10c-d, average pore size ranged between 11.9 µm and 33.0 µm. The smallest average pore size was observed under high LP, high SS, and high PF settings. Sample S12 (1500 W LP, 10 mm/s SS, 4.5 rev/min PF) had the smallest average pore size (11.9 µm), whereas sample S1 (1200 W, 6 mm/s, 3.5 rev/min) had the largest (33.0 µm), about 177% larger than that of S12. Fig. 10e-f shows that maximum pore size decreases with increasing SED, but has no clear relationship with PFD. At low LP (1200 W), maximum pore size decreased as SS and PF increased (S1 → S3), while at high LP (1500 W), the maximum pore size increased with SS and PF (S10 → S12). The sample with the largest maximum pore (S1) had a value 240% higher than that of S10. These findings reveal the complex interactions of process parameters on porosity formation in LMD and highlight the importance of optimizing manufacturing conditions.

ANOVA results for porosity are shown in Fig. 11a-b, which illustrate the effects of LP, SS, and PF on porosity density and maximum pore size. The numerical contributions of these effects are detailed in TABLE 6. According to the analysis, the most dominant factor affecting both porosity density and maximum pore size is LP. The general trend is that both decrease as LP increases. However, a slight increase in maximum pore size was observed when LP was increased from 1400 W to 1500 W, contrary to the overall trend. The effects of SS and PF on

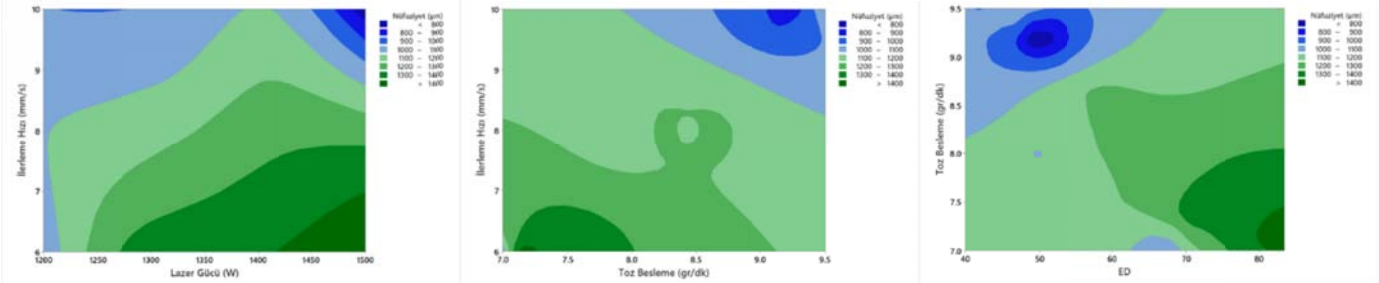

Fig. 9. Pareto analysis for factor *D* (%)

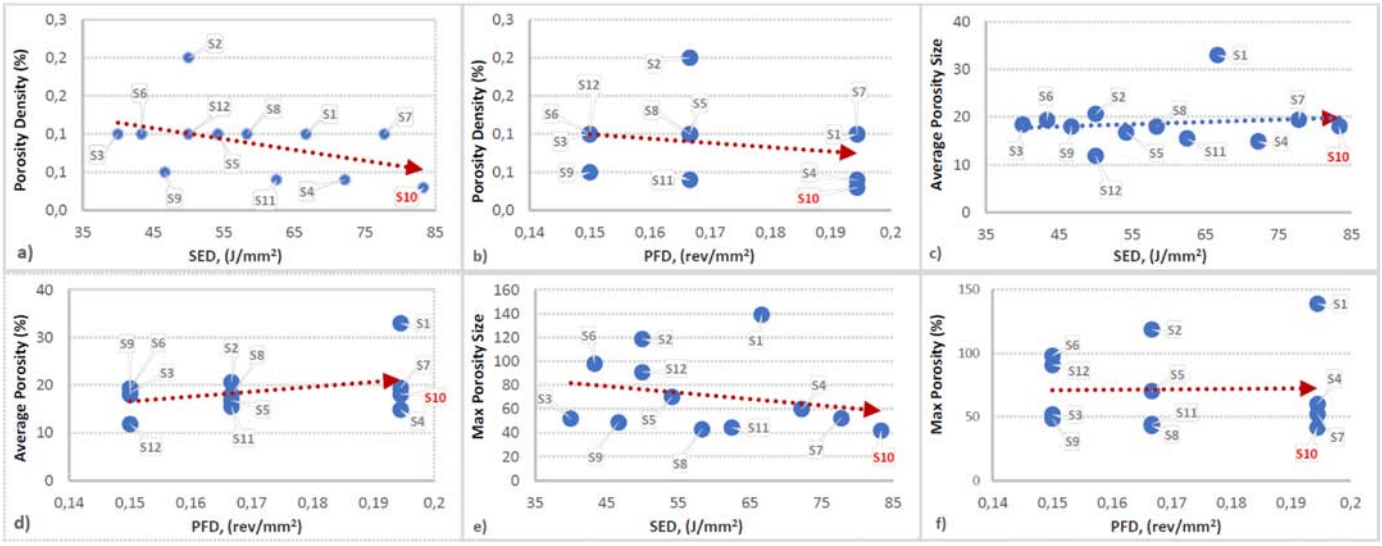

Fig. 10. Effect of SED and PFD on a) and b) Porosity Density (%) (η), c) and d) Average Porosity Size and e) and f) Max Porosity Size

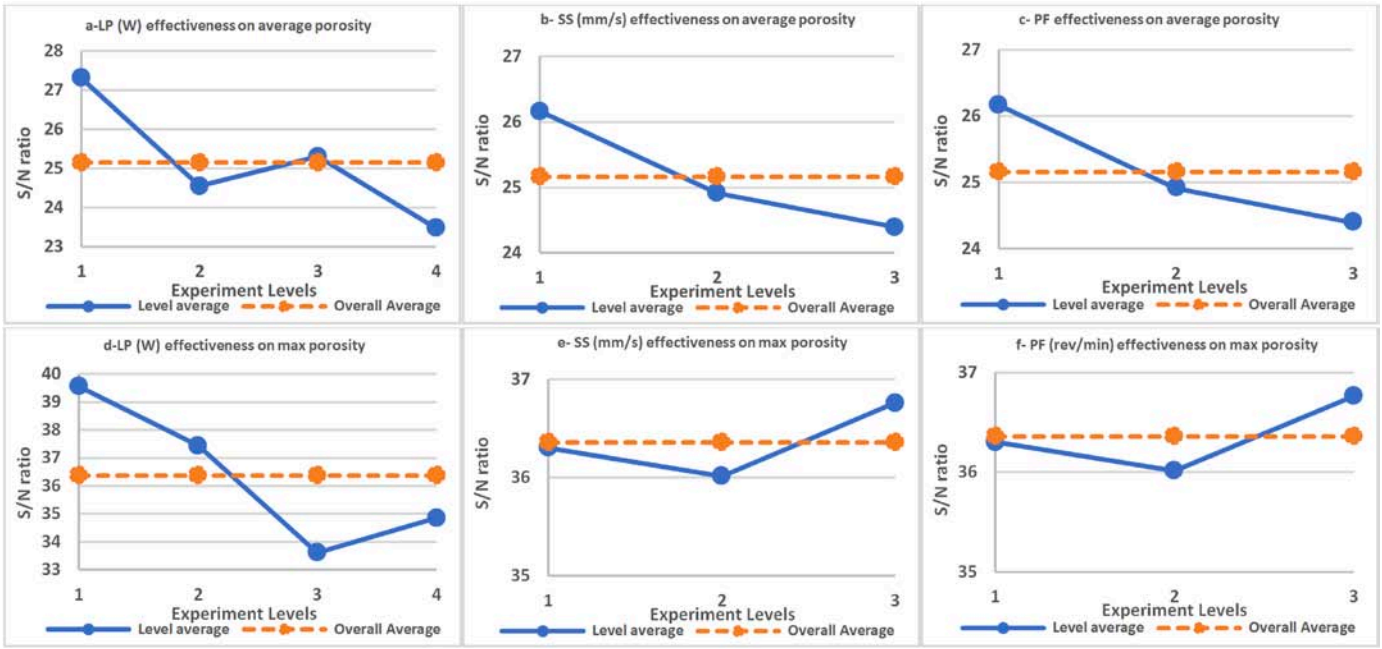

Fig. 11. Main effects plot for average porosity and max porosity

maximum pore size were quite limited, each contributing on the order of ~1%.

Fig. 12 shows a map that can help select the right combination of manufacturing parameters to optimize the porosity density of the coating. When the Pareto analysis is examined, the combined effects of LP and SSs are evaluated, it is seen that the lowest porosity density can be achieved when high LP (1500 W) and low SS (6 mm/s) are used. It is also observed

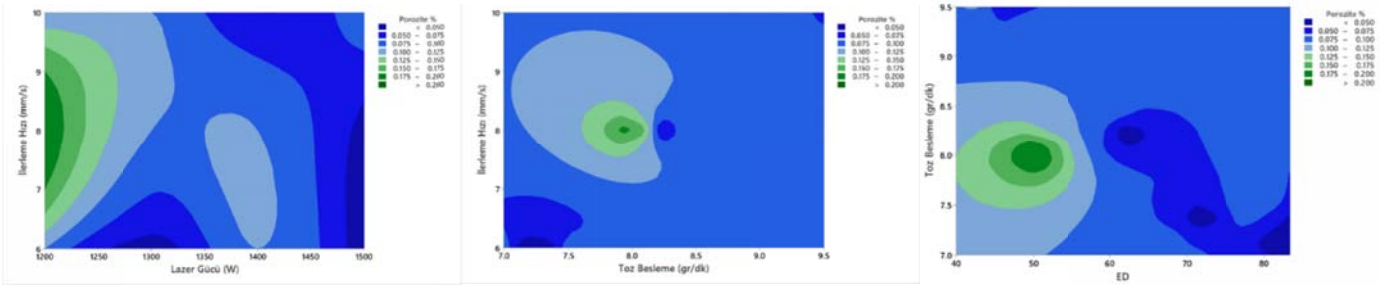

Fig. 12. Pareto analysis for factor porosity density

TABLE 6

Results of ANOVA for average porosity and max porosity

S/N ratio	25.16	**Effectiveness of process parameters on average porosity (µm)**							
	Degrees of Freedom	Average S/N Values				Sum of Squares	Variance	F	Percentage of Contribution (%)
		Level 1	Level 2	Level 3	Level 4				
A – LP	3	27.31	24.55	25.31	23.47	23.65	7.88	2.88	45.78
B – Scan Speed	2	26.16	24.92	24.40		6.60	3.30	1.20	19.16
C – PF	2	26.16	24.92	24.40		6.60	3.30	1.20	19.16
Error	4					10.95	2.74		15.90
Total	11					47.79	17.22		100.00
S/N ratio	36.36	**Effectiveness of process parameters on max porosity (µm)**							
	Degrees of Freedom	Average S/N Values				Sum of Squares	Variance	F	Percentage of Contribution (%)
		Level 1	Level 2	Level 3	Level 4				
A – LP	3	39.55	37.44	33.60	34.85	63.65	21.22	1.07	50.33
B – Scan Speed	2	36.30	36.02	36.76		1.14	0.57	0.03	1.35
C – PF	2	36.30	36.02	36.76		1.14	0.57	0.03	1.35
Error	4					79.20	19.80		46.97
Total	11					145.13	42.16		100.00

that at low powder feed rates, the porosity density decreases as SED increases.

3.3. Development of statistical models

Parameter optimization study was performed using the response surface method with the porosity, efficiency, and penetration outputs obtained from the experimental design parameters and analyzes given in TABLE 7. LP, feed rate, and powder feed rate parameters constitute the input values. Each target output was seen to have equal value in the desirability function. Targeted outputs are shown in TABLE 8. It was concluded that the production parameters of S10 were the most optimum.

According to the analytical methods described above, the RSM model was established. ANOVA was performed with a stepwise mode that can automatically eliminate insignificant terms. After eliminating insignificant terms, the final empirical model regarding efficiency, %*D* and Porosity in terms of coded factors is as follows:

$$\eta(\%) = -4.29 - 0.1496\mathrm{LP} - 23.4\mathrm{SS} + 47.1\mathrm{PF} + \\ + 0.000041\mathrm{LP}^2 - 1.615\mathrm{SS}^2 - 6.54\mathrm{PF}^2 - \\ + 0.00435\mathrm{LP}\times\mathrm{SS} + 0.00864\mathrm{LP}\times\mathrm{PF} + \\ + 6.51\mathrm{SS}\times\mathrm{PF} \quad (5)$$

$$D(\%) = -75390 + 788\mathrm{LP} + 101758\mathrm{SS} - 202379\mathrm{PF} - \\ + 0.232\mathrm{LP}^2 + 6742\mathrm{SS2} + 27335\mathrm{PF}^2 + \\ + 16.3\mathrm{LP}\times\mathrm{SS}\ \mathrm{LP}\times\mathrm{PF} - 27194\mathrm{SS}\times\mathrm{PF} \quad (6)$$

$$\mathrm{Porosity}(\%) = 43.6 + 0.012\mathrm{LP} + 12.6\mathrm{SS} - 25\mathrm{PF} + \\ + 0.000001\mathrm{LP}^2 + 0.90\mathrm{SS}^2 + 3.5\mathrm{PF}^2 + \\ + 0.0019\mathrm{LP}\times\mathrm{SS} - 0.0036\ \mathrm{LP}\times\mathrm{PF} - \\ + 3.6\ \mathrm{SS}\times\mathrm{PF} \quad (7)$$

TABLE 7

Targeted outputs

Output	Target	Lower Limit	Target	Upper Limit	Weight	Importance
Efficiency %	Maximum	0.583	0.79		1	1
Penetration (µm)	Specific Target	7.2	14.5		1	1
Maximum Porosity Size (µm)	Minimum		41.79	139.04	1	1
Average Porosity Size (µm)	Minimum		11.88	32.97	1	1
Porosity %	Minimum		0.03	0.20	1	1

TABLE 8

Optimum parameters obtained as a result of the solution

Parameter	Optimum calculated optimum	Optimum parameter
LP (W)	1481.21	1500
SS (mm/s)	6.15	6
PF (gr/min)	3.49	3.5

The regression models developed for efficiency (η), dilution ratio (D), and porosity provide both statistical fit and metallurgical interpretation. For efficiency (η), the linear coefficient of LP (LP: –0.1496) is negative, suggesting that efficiency decreases with increasing power when considered in isolation. However, the quadratic term LP^2 (+0.000041) indicates a nonlinear relationship, where efficiency improves at higher power levels due to more stable melt pools and better powder absorption. Scan speed (SS: –23.4) exhibits the strongest negative effect, confirming that faster scanning sharply reduces efficiency. Powder feed rate (PF: +47.1) strongly enhances efficiency, but its quadratic term (–6.54) shows diminishing returns at very high feed levels. Among interaction terms, LPPF (+0.00864) demonstrates a synergistic effect, while LPSS (+0.00435) compensates partially for the negative effect of speed. These findings are supported by ANOVA results, which attribute ~32% contribution each to scan speed and powder feed, and ~22% to LP.

For dilution ratio (D), the positive coefficient of LP (+788) indicates that higher power increases dilution by deepening penetration. Similarly, SS (+101758) enhances dilution through narrower, deeper melt pools. In contrast, PF (–202379) significantly reduces dilution by providing additional material that lowers substrate melting. Quadratic terms (e.g., PF^2 = +27335) indicate that excessive powder may destabilize the melt pool and increase dilution. Interaction terms such as LPSS (+16.3) amplify dilution, while LPPF (–27194) and SS*PF (–27194) confirm that powder feed mitigates dilution when combined with higher energy input or scan speed. This explains the experimentally observed dilution variation between ~9.7% (S12) and 14.5% (S10).

For porosity, LP (+0.012) exerts a slight positive effect, attributed to keyhole pore formation at excessive energy input. SS (+12.6) significantly increases porosity due to insufficient gas escape at high speeds, while PF (-25) reduces porosity by stabilizing melt pool filling. The quadratic term PF^2 (+3.5) suggests porosity reappears at very high powder feeds due to incomplete melting. Interaction effects further refine these trends: LPSS (+0.0019) increases porosity, whereas LPPF (–0.0036) and SS*PF (–3.6) mitigate it. These predictions are consistent with experimental results, where porosity varied from 0.03% (S10) under high power and low speed to 0.10% (S12) under low power and higher speeds. ANOVA further confirms that LP is the most influential parameter (~46% for average porosity and ~50% for maximum porosity).

Overall, the model coefficients not only fit the experimental data but also align with physical expectations of melt pool behavior. The negative coefficients (e.g., SS for η, PF for D) identify detrimental effects, while quadratic and interaction terms highlight the non-linear and synergistic behaviors inherent to LMD. This integrated approach confirms both the practical significance of coefficients and the predictive reliability of the developed models.

3.4. Microstructural analysis

The microstructure images of 12 samples produced in multilayers using a single weld seam under 100× and 500× magnifications are shown in Fig. 13. In the 100× magnification images in Fig. 13, it is seen that $\alpha + \beta$ phase mixtures are present. The β phase ratio varies in these samples; therefore, grain size analysis was performed by the Differential Interference Contrast (DIC) method in Fig. 14a. TABLE 4 shows the changes in average β phase grain sizes according to the samples. In all samples, the columnar grains observed in the lower layer give way to smaller equiaxed grains in the upper layers. No significant trend was observed between the β phase grain sizes detected in the etched microstructure images and the LP, SS and feed speed. It has been evaluated that these grain sizes are the primary grains that first solidify from the liquid and that possible microstructural differences can be eliminated due to the high instantaneous heat input they are exposed to during the subsequent passes in the multilayer laser additive manufacturing process. When examined in general, it is seen that the microstructures of the samples are largely similar. Ti6Al4V, an $\alpha + \beta$ phase alloy, formed its final microstructure at room temperature by first solidifying the primary beta grains during the cooling stage after laser deposition and then transforming these beta grains into the α or martensite phase. In all samples, a martensitic structure with a needle morphology was observed together with the β phase.

DIC was used for beta grain size distribution. Grain size analysis was performed with DIC as shown in Fig. 14a for each sample and average grain sizes were determined. The changes in the average sizes of beta grains colored red with SED and PFD are given in Fig. 14b. When the average β phase grain sizes are examined, no significant difference is seen. Therefore, it can be said that all parameters are very close to each other.

LP, SS, and PF jointly define the SED and PFD, which directly control the solidification conditions during LMD and therefore the resulting phase transformations in Ti6Al4V. At relatively low SED values (e.g., S1-S3), the high cooling rates promote the formation of acicular α' martensite within prior β grains, as expected under rapid non-equilibrium solidification. This martensitic morphology explains the high hardness but poor ductility of samples produced under such conditions. As SED increases (S4-S6), partial decomposition of α' martensite into finer basket-weave α variants is observed, reflecting the transition from diffusionless to diffusion-controlled phase transformation due to reduced cooling rates. At higher SED (S7-S10), the thermal input is sufficient to promote the growth of lamellar α colonies with basket-weave structures, accompanied by clearer β grain boundary delineation. This morphology enhances plasticity by providing multiple slip paths while reducing residual stresses, though it leads to a moderate decrease in strength compared to martensitic structures. At the highest SSs (S9, S12), despite high LP, the effective SED decreases, resulting again in finer α′ martensite due to accelerated cooling, together with increased porosity from unstable melt pool dynamics. Thus, the progression from α'-dominated microstructures at low SED to basket-weave α morphologies at high SED illustrates the strong correlation between process parameters, phase transformation pathways (α' : lamellar α), and the balance of mechanical properties.

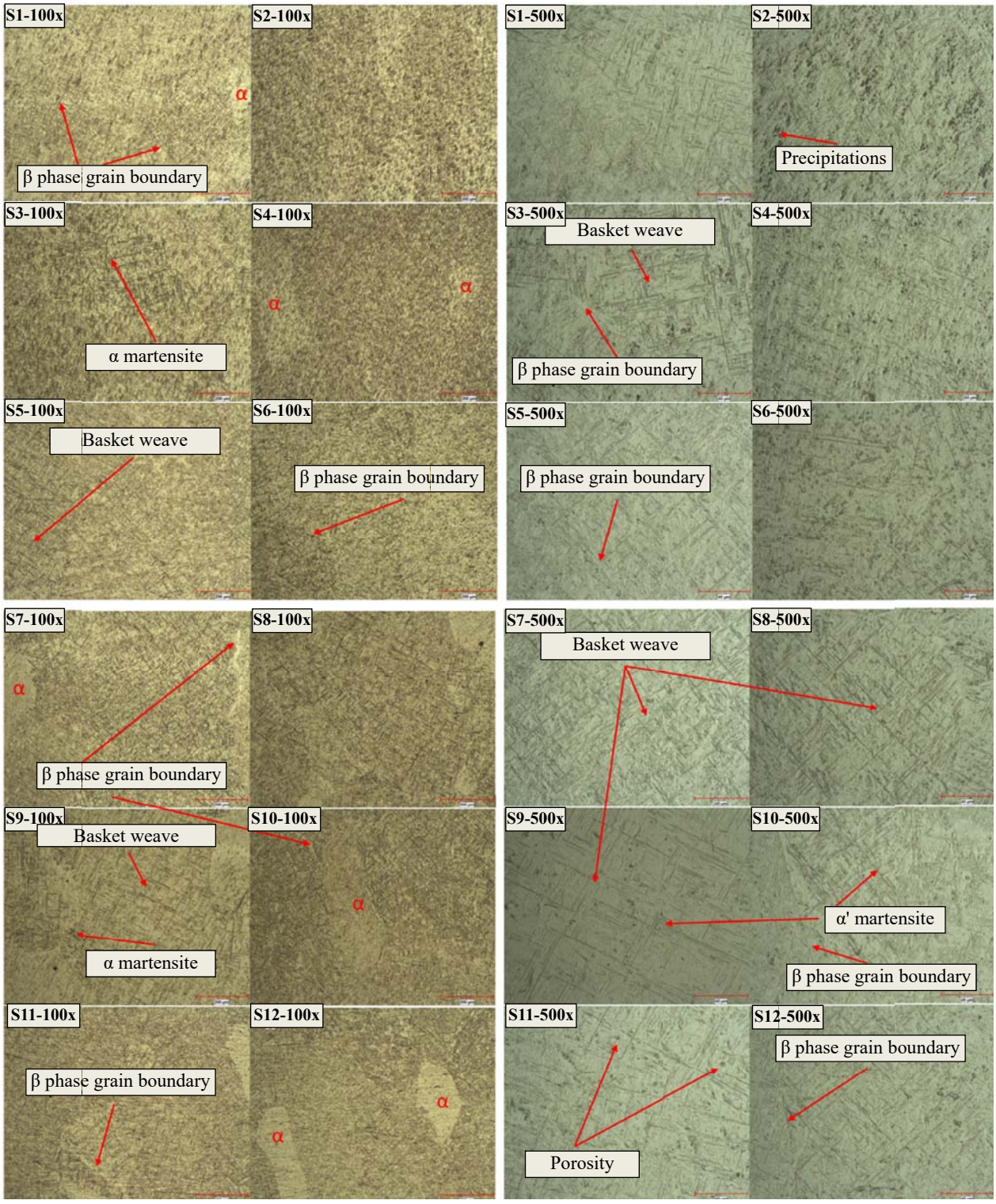

Fig. 13. Microstructure of samples produced by LMD method with 12 different parameters

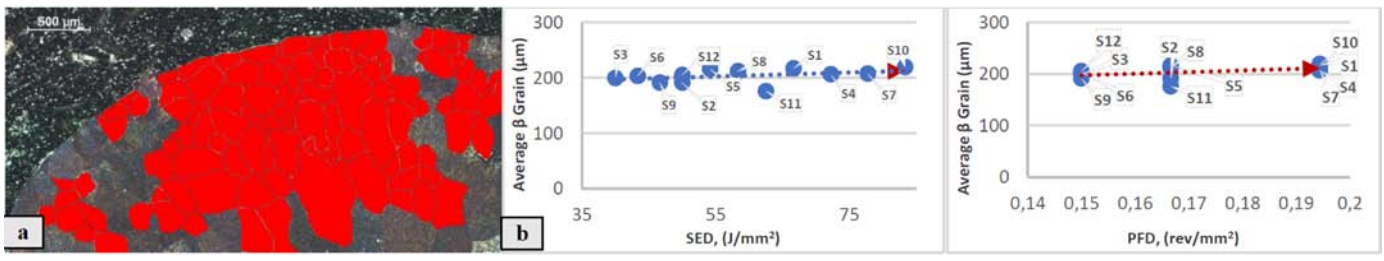

Fig. 14. a) Grain size distribution by DIC, b) Average *β* phase grain size

3.5. Mechanical properties

3.5.1. Hardness analysis

The average microhardness values of the samples (HV, 50 g load) were measured across 6 levels through the build height, and the results are presented in Fig. 15. Examination of the microhardness profiles revealed no significant hardness change between layers overall. However, a relative increase in hardness was observed at level 2 (near the base of the build).

In theory, microhardness is expected to correlate with cooling rate and β-phase content. Due to cyclic thermal processes in additive manufacturing, some β phase retention is inevitable, and more β is expected in lower layers [41]. Consistently, when microhardness variation by layer level was examined, higher microhardness values were obtained in the lower levels. This can be explained by the thermal dynamics of the LMD process: the level 2 region, close to the substrate, experiences faster solidification and thus finer grain structure. According to the Hall-Petch relationship, this finer microstructure contributes to higher hardness at level 2 [42]. In contrast, relatively slower cooling and smaller thermal gradients in the upper layers lead to a coarser microstructure with larger grains, resulting in lower hardness in the top layers. These observations highlight the significant effect of layer position on microstructure and mechanical properties in additive manufacturing. No significant horizontal hardness variation was observed, which is expected for single-track walls and indicates that process parameters produced a fairly homogeneous effect across the layer width.

The average hardness distributions of the samples are shown in Fig. 16a, and the effects of SED and PFD on microhardness are shown in Figs. 16b-c. All samples had average hardness values in the narrow range of 354-365 HV. This indicates that the process parameters did not cause a statistically significant change in average hardness.

No significant effect of increasing LP on microhardness was observed. However, increasing SED caused a slight decrease in average hardness. This can be explained by the fact that higher energy input promotes grain growth, thereby slightly reducing hardness. On the other hand, PFD showed no significant effect on hardness.

3.5.2. Tensile properties

Sample S10 was identified as having the best as-built results in terms of efficiency, penetration, and porosity. To further optimize the microstructure of this sample and reduce porosity, the sample underwent HIP followed by HT, and also cryogenic processing (CP).

To investigate the effects of the As-Built (AB), HIP+HT, and CP (24 h, 36 h) processes on mechanical properties, tensile specimens were prepared from the bottom (N1), middle (N2), and top (N3) regions of walls produced with the S10 parameters. The results are presented in TABLE 9 and Fig. 17.

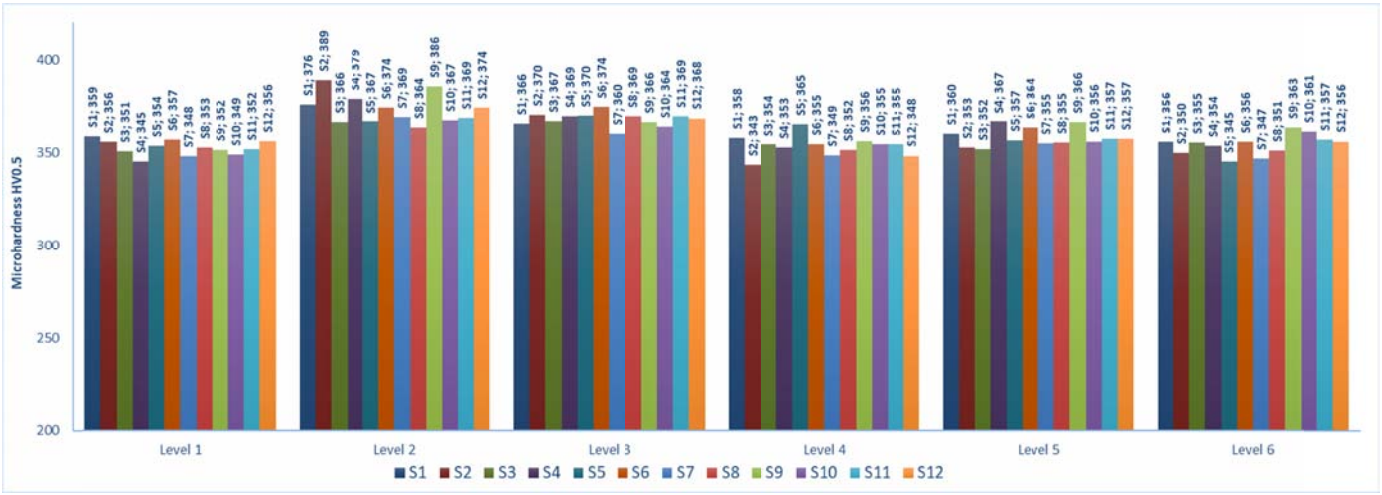

Fig. 15. Average microhardness values of the sample produced with 12 different parameters in 6 layers

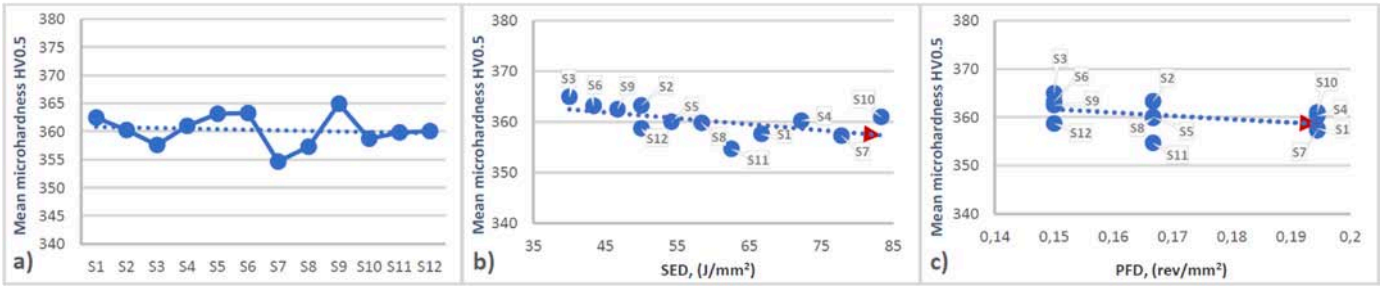

Fig. 16. a) The average hardness distributions of the samples, b) the effects of SED and c) PFD parameters on microhardness

TABLE 9

Effect of AB, HIP-HT and CP (24 h, 36 h) on mechanical properties

	Ultimate strength (MPa)	Yield strength (MPa)	Strain (%)
AB-N1	1201	1157	3.96
AB-N2	1228	1095	2.85
AB-N3	1259	1153	1.81
HIP and HT-N1	959	931	6.08
HIP and HT-N2	953	912	6.4
HIP and HT-N3	973	972	1.04
CP-24 h-N1	964	908	7.6
CP-24 h-N2	960	908	7.26
CP-24 h-N3	1075	1021	1.83
CP-36 h-N1	962	905	7.5
CP-36 h-N2	978	892	7.8
CP-36 h-N3	1053	987	3.2

The microstructure of titanium alloys varies depending on the temperature and cooling rates to which they are exposed [44]. Martensite and β phases provide high hardness while reducing the extensibility of the material. The low elongation values of the samples produced with LMD indicate that β and martensite phases are dominant in the structure. Cyclic heating and cooling in the LMD process leads to multiple changes in the microstructure [45]. Insufficient cooling rate prevents α and martensitic transformation and causes the β phase to be preserved. When AB and heat-treated samples were compared, a decrease in the tensile and yield strengths of the samples was observed after heat treatment. On the other hand, the elongation at break, which is an indicator of the toughness of the material, increased significantly. The effect of cryogenic treatment (24 and 36 hours) on tensile and yield strength was limited compared to the HIP-HT treatment [46]. However, cryogenic treatment significantly affected the elongation at break. For example, the elongation at break of the N1 sample in the bottom layer reached 7.6% after 24-hour cryogenic treatment; this value was measured as 3.9% in the AB sample and 6% after the HIP-HT. Although the effects of 24 and 36-hour cryogenic treatments on the elongation at break were generally similar, the 36-hour treatment in the S3 sample in the top layer provided approximately 73% higher elongation at break compared to the 24-hour treatment.

HIP reduces porosity in the material, increases density and homogenizes the microstructure [47]. However, the residual stresses and microstructural changes resulting from this treatment may have negative effects on ductility and elongation at break.

Cryogenic HT applied following the HIP treatment reduces residual stresses in the internal structure and stabilizes the microstructure. Cryogenic temperatures promote the completion of the martensitic transformation and finer and more homogeneous precipitation of carbides [31]. This situation contributes to the improvement of the elongation at fracture by increasing the ductility of the material. After the cryogenic treatment, the energy absorption capacity and deformation ability of the material are increased due to the decreased internal stresses and more balanced microstructure. As a result, the cryogenic HT applied after the HIP process led to a significant increase in the elongation at fracture of the samples.

The mechanical test results confirm the strong influence of microstructural evolution on the performance of Ti6Al4V produced by LMD and subjected to post-processing. In the AB condition, ultimate tensile strength reached up to 1259 MPa (N3), with yield strength values above 1095 MPa. However, the strain to failure remained very limited (1.81-3.96%). This behavior is directly attributable to the dominant presence of α' martensite within the microstructure, which increases strength but reduces ductility due to its acicular morphology and limited slip systems.

After HIP and heat treatment, the mechanical response changed significantly. The UTS decreased to the range of 953-973 MPa, and the yield strength stabilized around 912-972 MPa. However, elongation improved substantially, with values rising to 6.08-6.40% for N1 and N2. This transition can be explained by the reduction of porosity (as observed in TABLE 4, from ~0.10% to ~0.03-0.04% in optimized conditions) and the transformation of α' martensite into a lamellar $\alpha + \beta$ structure. The lamellar morphology promotes dislocation movement and crack deflection, thereby enhancing plasticity at the expense of

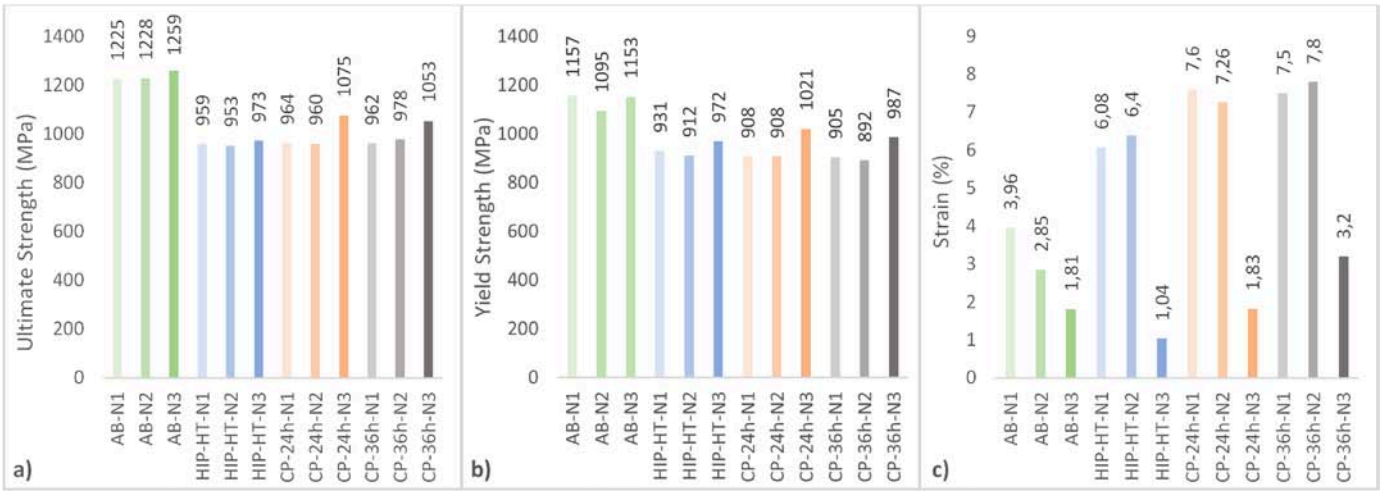

Fig. 17. Effect of a) AB, b) HIP-HT and c) CP (24h, 36 h) on mechanical properties

strength. Interestingly, sample N3 still exhibited low elongation (1.04%), suggesting microstructural heterogeneity or insufficient pore closure under HIP at that parameter set.

The application of cryogenic treatment provided an additional improvement in the balance of properties. After 24 h cryogenic treatment, elongation increased further to 7.26-7.60% (N1-N2), while maintaining strength levels close to 960-1075 MPa. This indicates that cryogenic exposure effectively relieved residual stresses and refined α/β interfaces, contributing to improved plasticity without a significant loss of strength. With 36 h cryogenic treatment, ductility was again enhanced (up to 7.8%), and mechanical stability was achieved across the samples. For instance, N2 exhibited 978 MPa ultimate tensile strength, 892 MPa yield strength, and 7.8% elongation, representing a highly balanced performance. However, in certain conditions (e.g., N3 samples), strength recovery was more pronounced (1053-1075 MPa), accompanied by moderate ductility (1.83-3.2%), highlighting the sensitivity of cryogenic exposure to microstructural state and processing history.

3.6. Microstructure Examination and Porosity Measurement After Post-Processing

Fig. 18 shows the cross-sectional images taken from the tensile test samples. In the microstructure examination of the sample produced with LMD and without post-processing, seen in Fig. 18a, large-sized porosities are noticeable. In the microstructure, in addition to the light-colored α phase, dark-colored β phases are noticeable. Grain boundaries are distinct and grain sizes are large. Secondary α phases were formed in the LMD process, and phase structures that distributed in different directions were formed as a result of cooling in the β region in air. When controlled cooling is applied above the β transus temperature during HIP and heat treatment, β and martensitic α' needle structures are formed in addition to α phases, as seen in Fig. 18b. Since the β transus temperature cannot be exceeded much, a part of the β phase has transformed into lamellar needle-shaped α phases due to the cooling in the $\alpha + \beta$ phase region [41]. This transformation may cause some decrease in the strength of the material [48]. After cryogenic treatment, as seen in Fig. 18c, primary β grain boundaries are destroyed and α grain boundaries are shortened in multiple directions and form the structure called "basket-weave" [26]. Basket-weave structure generally provides higher ductility; therefore, fracture toughness and fatigue resistance may be increased. The study shows that α' martensite has the highest strength value among all microstructures. The strength of columnar $\alpha + \beta$ microstructure is generally higher than that of equiaxed $\alpha + \beta$. However, there is usually a trade-off between strength and ductility. Fine needle-shaped α' martensite provides high strength but causes a decrease in plasticity.

It was observed that after cryogenic treatment, the martensite structure transformed into a basket weave structure by reducing the grain boundaries, increasing the plasticity with-

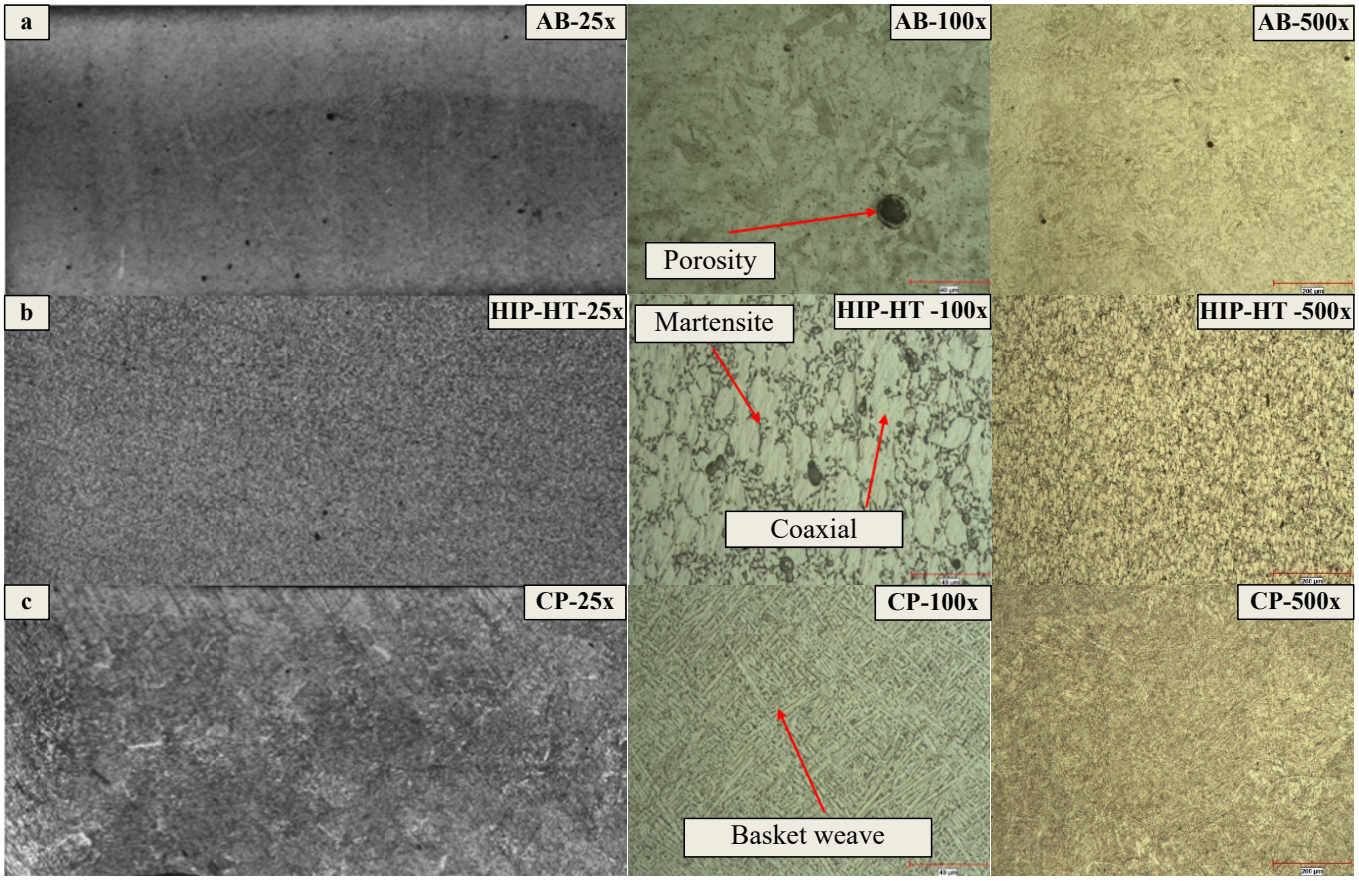

Fig. 18. Cross-Sectional view taken from tensile test samples a) AB, b) HIP-IT and c) CP

out causing a significant change in strength. This shows that cryogenic treatment can be an effective method to optimize the mechanical properties of Ti6Al4V alloy.

Microstructural analyses revealed the presence of porosity at the macroscopic level in the untreated sample. After the HIP process, a statistically significant decrease in porosity levels was observed. This result results from the HIP process being carried out under high pressure (usually 100-200 MPa) and high temperature (usually 60-70% of the material's melting point) conditions. The HIP process significantly reduces the amount of porosity by closing the voids in the material and densifying the microstructure. When the effect of the CP on porosity was examined, no statistically significant change was observed in the general porosity level. However, a partial decrease in porosity was detected in the tensile test area. This shows that the CP can cause microstructural changes, but this effect is limited to porosity. However, it was determined that 24- and 36-hour periods did not have a significant effect on porosity density.

The data presented in Fig. 19 shows the porosity values of three different samples comparatively. There is an approximately three-fold difference between the HIP-HT and AB samples. This result emphasizes the critical importance of HIP application in terms of porosity control in parts produced by the LMD method. Studies in the literature confirm that the HIP process largely eliminates porosities. It has been observed that cryogenic treatment contributes to the organization of the microstructure and the increase of the ductility of the material. This effect is due to the completion of the martensitic transformation, the decrease of the dislocation density, and the finer and more homogeneous distribution of secondary phases.

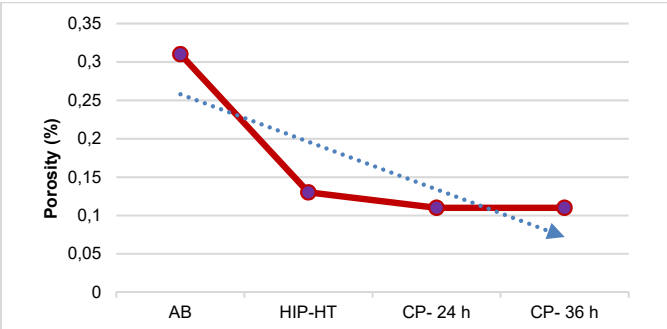

Fig. 19. Results of full cross-section porosity measurements of tensile samples with post-processing

4. Conclusion

The main purpose of this study was to optimize the production of large-sized aerospace components with high reliability and superior mechanical performance from Ti6Al4V alloy using a LMD system. For this purpose, process parameters were systematically investigated and optimized, and the influence of post-processing treatments, including HIP and cryogenic treatment, on the final properties of the alloy was examined in detail. The findings demonstrate clear correlations between process parameters, microstructural evolution, porosity characteristics, and mechanical behavior.

Coating height was positively correlated with SED and PFD, with an increase of 40 J/mm^2 in SED producing a 29% rise in coating height. The correlation coefficient between SED and efficiency (R = 0.93) confirmed a strong relationship, while the dilution ratio increased proportionally with both SED and PFD, ranging between 9.7% and 14.5%. Increasing LP improved efficiency by ~22%, whereas higher SS and powder feeding rates reduced it by ~32%. The highest efficiency (>76%) was achieved under high LP (1500 W) and low SS (6 mm/s). Although LP had only a weak effect on coating height (0.15%), SS and powder feeding exerted a significant negative influence of ~40%. The maximum coating height (8.8 mm) was obtained at 1300 W, 6 mm/s, and 3.5 rev/min. Dilution was affected almost equally by all three parameters; higher SSs produced shallow penetration and poor spreading, whereas increased SED at constant powder flow raised dilution.

Porosity analysis revealed that increasing SED and PFD reduced porosity density, while slightly increasing average pore size. The lowest porosity density (~3%) occurred at the highest SED, with pore sizes varying between 11.9 µm and 33.0 µm. Maximum pore size decreased with SED but showed no direct correlation with PFD. ANOVA confirmed LP as the most dominant factor affecting porosity density and pore size. Optimal porosity results were obtained at 1500 W LP, 6 mm/s SS, and 3.5 rev/min powder feed rate.

Microstructural evaluation revealed $\alpha + \beta$ phase mixtures in all samples, with columnar grains in the lower layers and smaller equiaxed grains in the upper regions. Martensitic α' needles were consistently observed, confirming the sensitivity of LMD cooling rates to phase transformation. The microstructural features were directly reflected in the mechanical behavior. Martensitic microstructures in the AB condition resulted in very high strength but low ductility. HIP processing transformed the microstructure into a lamellar α/β morphology, which significantly reduced porosity, homogenized the structure, and doubled the elongation at break, though tensile and yield strength were slightly reduced due to lamellar coarsening. Subsequent cryogenic treatment stabilized α/β interfaces and transformed the microstructure into a basket-weave morphology, which enhanced ductility (up to ~7.6% in N1 samples), maintained strength, and further reduced porosity density by nearly threefold. This microstructural tailoring also improved toughness and fatigue resistance potential by relaxing residual stresses.

Overall, this systematic investigation demonstrates the combined role of process parameter optimization and advanced post-processing in tailoring the properties of LMD-fabricated Ti-6Al-4V. Unlike earlier studies that considered only parameter effects or conventional post-processing individually, the present study provides a holistic evaluation, linking process parameters to porosity control, microstructure, and mechanical response under different post-treatment conditions. The combined HIP and cryogenic route emerge as a particularly effective strategy, offering a balanced improvement in both strength and ductility

while ensuring low porosity. These findings provide practical guidelines for producing reliable, defect-controlled, and mechanically robust aerospace components by LMD. Future work should address long-term fatigue and tribocorrosion performance, integration of in-situ monitoring, and scaling the optimized treatments to larger and more complex geometries to further support industrial implementation in aerospace and defense applications.

REFERENCES

[1] A. Gasser, G. Backes, I. Kelbassa, A. Weisheit, K. Wissenbach, Laser Additive Manufacturing. Laser Tech. J. **7** (2), 58-63 (2010). DOI: https://doi.org/10.1002/LATJ.201090029

[2] S. Konovalov, et al., Surface modification of Ti-based alloy by selective laser melting of Ni-based superalloy powder. J. Mater. Res. Technol. **9** (4), 8796-8807 (2020). DOI: https://doi.org/10.1016/j.jmrt.2020.06.016

[3] D. Herzog, V. Seyda, E. Wycisk, C. Emmelmann, Additive manufacturing of metals. Acta Mater. **117**, 371-392 (2016). DOI: https://doi.org/10.1016/j.actamat.2016.07.019

[4] C.S. Wang, et al., Multistep low-to-high-temperature heating as a suitable alternative to hot isostatic pressing for improving laser powder-bed fusion-fabricated Ti-6Al-2Zr-1Mo-1V microstructural and mechanical properties. Mater. Sci. Eng. A **841**, 143022 (2022). DOI: https://doi.org/10.1016/j.msea.2022.143022

[5] S.M. Thompson, L. Bian, N. Shamsaei, A. Yadollahi, An overview of Direct Laser Deposition for additive manufacturing; Part I: Transport phenomena, modeling and diagnostics. Addit. Manuf. **8**, 36-62 (2015). DOI: https://doi.org/10.1016/j.addma.2015.07.001

[6] T. DebRoy et al., Additive manufacturing of metallic components – Process, structure and properties. Prog. Mater. Sci. **92**, 112-224 (2018). DOI: https://doi.org/10.1016/j.pmatsci.2017.10.001

[7] C. Tan, K. Zhou, W. Ma, P. Zhang, M. Liu, T. Kuang, Microstructural evolution, nanoprecipitation behavior and mechanical properties of selective laser melted high-performance grade 300 maraging steel. Mater. Des. **134**, 23-34 (2017). DOI: https://doi.org/10.1016/j.matdes.2017.08.026

[8] E.T. Burkhart, L. Hefti, Advancements of Superplastic Forming and Diffusion Bonding of Titanium Alloys for Heat Critical Aerospace Applications. SAE Tech. Pap. 2020-March (March), 1–7 (2020). DOI: https://doi.org/10.4271/2020-01-0033

[9] T. Wahlström, J. Sahlström, Additive Manufacturing in Production: For the Automotive Industry. 20-40 (2016).

[10] R.M. Mahamood, E.T. Akinlabi, Effect of Laser Power and Powder Flow Rate on the Wear Resistance Behaviour of Laser Metal Deposited TiC/Ti6Al4V Composites. Mater. Today Proc. **2** (4-5), 2679-2686 (2015). DOI: https://doi.org/10.1016/j.matpr.2015.07.233

[11] L.E. Murr et al., Microstructure and mechanical behavior of Ti-6Al-4V produced by rapid-layer manufacturing, for biomedical applications. J. Mech. Behav. Biomed. Mater. **2** (1), 20-32 (2009). DOI: https://doi.org/10.1016/j.jmbbm.2008.05.004

[12] B. Vrancken, Study of Residual Stresses in Selective Laser Melting. PhD Thesis; KU Leuven Arenb. Dr. Sch. Fac. Eng. Sci. (June), 1-253 (2016).

[13] C. Zhong et al., Laser Metal Deposition of Ti6Al4V – A Brief Review. Appl. Sci. **10** (3), 764 (2020). DOI: https://doi.org/10.3390/app10030764

[14] D. Gu, Laser additive manufacturing of high-performance materials. (Lm) (2015). DOI: https://doi.org/10.1007/978-3-662-46089-4

[15] H. Aydin, M. Altay, A. Karşi, D. Ergin, A. Onayli, A. Bayram, Effect of Laser Cladding Parameters in Laser Direct Metal Deposition (LDMD) of Martensitic Stainless Steel Powder on Ductile Cast Iron. Lasers Eng. **52** (3), 87-106 (2022).

[16] Q. Liu et al., Microstructure and mechanical properties of LMD-SLM hybrid forming Ti6Al4V alloy. Mater. Sci. Eng. A **660**, 24-33 (2016). DOI: https://doi.org/10.1016/j.msea.2016.02.069

[17] T. Muslim, T. Karagoz, S. Kurama, P. Sezer, O.F. Yazici, R. Ozkok, Laser metal deposition of 17–4 PH stainless steel: Geometrical, microstructural, and mechanical properties investigation for structural applications. CIRP J. Manuf. Sci. Technol. **41**, 69-79 (2023). DOI: https://doi.org/10.1016/j.cirpj.2022.12.010

[18] J. Dutta Majumdar, A. Kumar, L. Li, Direct laser cladding of SiC dispersed AISI 316L stainless steel. Tribol. Int. **42** (5), 750-753 (2009). DOI: https://doi.org/10.1016/j.triboint.2008.10.016

[19] P. Shayanfar, H. Daneshmanesh, K. Janghorban, Parameters Optimization for Laser Cladding of Inconel 625 on ASTM A592 Steel. J. Mater. Res. Technol. **9** (4), 8258-8265 (2020). DOI: https://doi.org/10.1016/j.jmrt.2020.05.094

[20] S. Zhang, X. Lin, J. Chen, W. Huang, Heat-treated microstructure and mechanical properties of laser solid forming Ti-6Al-4V alloy. Rare Met. **28** (6), 537-544 (2009). DOI: https://doi.org/10.1007/S12598-009-0104-5

[21] Y. Liao, J. Bai, F. Chen, G. Xu, Y. Cui, Microstructural strengthening and toughening mechanisms in Fe-containing Ti-6Al-4V: A comparison between homogenization and aging treated states. J. Mater. Sci. Technol. **99**, 114-126 (2022). DOI: https://doi.org/10.1016/j.jmst.2021.04.063

[22] R.M. Mahamood, Effect of Laser Power and Gas Flow Rate on Properties of Directed Energy Deposition of Titanium Alloy. Lasers Manuf. Mater. Process. **5** (1), 42-52 (2018). DOI: https://doi.org/10.1007/S40516-018-0052-8

[23] R.M. Mahamood, E.T. Akinlabi, S. Akinlabi, Laser power and Scanning Speed Influence on the Mechanical Property of Laser Metal Deposited Titanium-Alloy. Lasers Manuf. Mater. Process. **2** (1), 43-55 (2015). DOI: https://doi.org/10.1007/S40516-014-0003-Y

[24] H. Zhang et al., Complete fine-equiaxed β-columnar grains in laser direct energy deposition of Ti–6Al–4V parts. J. Mater. Res. Technol. **26**, 4059-4069 (2023). DOI: https://doi.org/10.1016/j.jmrt.2023.08.208

[25] G. Özer, A. Karaaslan, A Study on the Effects of Different Heat-Treatment Parameters on Microstructure – Mechanical Properties and Corrosion Behavior of Maraging Steel Produced by Direct Metal Laser Sintering. Steel Res. Int. **91** (10), 1-8 (2020). DOI: https://doi.org/10.1002/srin.202000195

[26] S. Tao et al., Effect of multi-stage heat treatment on the microstructure and mechanical properties of Ti–6Al–4V alloy deposited by high-power laser melting deposition. Mater. Sci. Eng. A **895**, 146226 (2024).
DOI: https://doi.org/10.1016/j.msea.2024.146226

[27] Z. Zou, M. Simonelli, J. Katrib, G. Dimitrakis, R. Hague, Refinement of the grain structure of additive manufactured titanium alloys via epitaxial recrystallization enabled by rapid heat treatment. Scr. Mater. **180**, 66-70 (2020).
DOI: https://doi.org/10.1016/j.scriptamat.2020.01.027

[28] C.L. Li et al., Realizing superior ductility of selective laser melted Ti-6Al-4V through a multi-step heat treatment. Mater. Sci. Eng. A **799**, 140367 (2021).
DOI: https://doi.org/10.1016/j.msea.2020.140367

[29] Z. Zhao, J. Chen, H. Tan, G. Zhang, X. Lin, W. Huang, Achieving superior ductility for laser solid formed extra low interstitial Ti-6Al-4V titanium alloy through equiaxial alpha microstructure. Scr. Mater. **146**, 187-191 (2018).
DOI: https://doi.org/10.1016/j.scriptamat.2017.11.021

[30] J. Lambarri, J. Leunda, V. García Navas, C. Soriano, C. Sanz, Microstructural and tensile characterization of Inconel 718 laser coatings for aeronautic components. Opt. Lasers Eng. **51** (7), 813-821 (2013). DOI: https://doi.org/10.1016/j.optlaseng.2013.01.011

[31] R. Seede, A. Mostafa, V. Brailovski, M. Jahazi, M. Medraj, Microstructural and microhardness evolution from homogenization and hot isostatic pressing on selective laser melted Inconel 718: Structure, texture, and phases. J. Manuf. Mater. Process. **2** (2), (2018). DOI: https://doi.org/10.3390/jmmp2020030

[32] A. Eklund, M. Ahlfors, Heat treatment of PM parts by Hot Isostatic Pressing. Met. Powder Rep. **73** (3), 163-169 (2018).
DOI: https://doi.org/10.1016/j.mprp.2018.01.001

[33] A. Shokrani, I. Al-Samarrai, S.T. Newman, Hybrid cryogenic MQL for improving tool life in machining of Ti-6Al-4V titanium alloy. J. Manuf. Process. **43**, 229-243 (2019).
DOI: https://doi.org/10.1016/j.jmapro.2019.05.006

[34] K. Arunprasath, A.V. Pandiyan, R. Nekin Joshua, M. Vijayakumar, V. Manikandan, Investigation on fusion of Boron Nitride reinforced aluminium composite by cryogenic milling. Mater. Today Proc. **66**, 658-664 (2022).
DOI: https://doi.org/10.1016/j.matpr.2022.03.542

[35] Y. Sun, M. Hao, Statistical analysis and optimization of process parameters in Ti6Al4V laser cladding using Nd:YAG laser. Opt. Lasers Eng. **50** (7), 985-995 (2012).
DOI: https://doi.org/10.1016/j.optlaseng.2012.01.018

[36] M.C. Bobadilla, R.L. Lorza, R.E. García, F.S. Gómez, E.P.V. González, Coagulation: Determination of Key Operating Parameters by Multi-Response Surface Methodology Using Desirability Functions. Water **11** (2), 398 (2019).
DOI: https://doi.org/10.3390/w11020398

[37] E.M. Lee, G.Y. Shin, H.S. Yoon, D.S. Shim, Study of the effects of process parameters on deposited single track of M4 powder based direct energy deposition. J. Mech. Sci. Technol. **31** (7), 3411-3418 (2017). DOI: https://doi.org/10.1007/s12206-017-0239-5

[38] P.R.A. Bloemer et al., Laser Cladding of Inconel 625 on AISI 316L: Microstructural and Mechanical Evaluation of Parameters Estimated by Empirical-Statistical Model. J. Mater. Eng. Perform. **31** (1), 211-220 (2022).
DOI: https://doi.org/10.1007/s11665-021-06147-8

[39] M. Ilanlou, R. Shoja Razavi, A. Nourollahi, S. Hosseini, S. Haghighat, Prediction of the geometric characteristics of the laser cladding of Inconel 718 on the Inconel 738 substrate via genetic algorithm and linear regression. Opt. Laser Technol. **156**, 108507 (2022). DOI: https://doi.org/10.1016/j.optlastec.2022.108507

[40] S. Jelvani, R. Shoja Razavi, M. Barekat, M. Dehnavi, Empirical-Statistical Modeling and Prediction of Geometric Characteristics for Laser-Aided Direct Metal Deposition of Inconel 718 Superalloy. Met. Mater. Int. **26** (5), 668-681 (2020).
DOI: https://doi.org/10.1007/s12540-019-00355-7

[41] A.R. Nassar, J.S. Keist, E.W. Reutzel, T.J. Spurgeon, Intra-layer closed-loop control of build plan during directed energy additive manufacturing of Ti-6Al-4V. Addit. Manuf. **6**, 39-52 (2015).
DOI: https://doi.org/10.1016/j.addma.2015.03.005

[42] Z. Zhou, Y. Liu, X. Liu, Q. Zhan, K. Wang, Microstructure evolution and mechanical properties of in-situ Ti6Al4V–TiB composites manufactured by selective laser melting. Compos. Part B Eng. **207**, 108567 (2021).
DOI: https://doi.org/10.1016/j.compositesb.2020.108567

[43] A. Lont, T. Poloczek, J. Górka, The structure and properties of laser-cladded Inconel 625/TiC composite coatings. Mater. Sci. Pol. **40** (4), 91-103 (2022).
DOI: https://doi.org/10.2478/msp-2022-0026

[44] R. Sabban, S. Bahl, K. Chatterjee, S. Suwas, Globularization using heat treatment in additively manufactured Ti-6Al-4V for high strength and toughness. Acta Mater. **162**, 239-254 (2019).
DOI: https://doi.org/10.1016/j.actamat.2018.09.064

[45] Y. Zhai, D.A. Lados, E.J. Brown, G.N. Vigilante, Fatigue crack growth behavior and microstructural mechanisms in Ti-6Al-4V manufactured by laser engineered net shaping. Int. J. Fatigue **93**, 51-63 (2016).
DOI: https://doi.org/10.1016/j.ijfatigue.2016.08.009

[46] P. Gao et al., Effect of heat treatment on microstructure and mechanical properties of Fe–Cr–Ni–Co–Mo maraging stainless steel produced by selective laser melting. Mater. Sci. Eng. A **814**, 141149 (2021).
DOI: https://doi.org/10.1016/j.msea.2021.141149

[47] S.L. Semiatin et al., Plastic flow and microstructure evolution during thermomechanical processing of laser-deposited Ti-6Al-4V preforms. Metall. Mater. Trans. A **32** (7), 1801-1810 (2001).
DOI: https://doi.org/10.1007/s11661-001-0156-0

[48] C. Murgau Charles, Microstructure model for Ti-6Al-4V used in simulation of additive manufacturing. Doctoral Thesis, Luleå University of Technology, Sweden (2016).